Journal of African Earth Sciences 214 (2024) 105244

Contents lists available at ScienceDirect

Journal of African Earth Sciences

journal homepage: www.elsevier.com/locate/jafrearsci

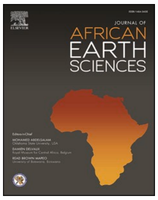

Multistage evolution of gold mineralization in the Kibali gold district: Insights from pyrite analyses

Yann Waku Mpaka [a,b,c,*], Bjorn P. Von der Heyden [a,**], Sarah Glynn [d,e], Gary Hurst [b], David Lawrence [b], Trézène Bampata [b], Etienne Mwandale [b]

[a] Department of Earth Sciences, Stellenbosch University, Private Bag X1, Matieland, 7602, South Africa
[b] Barrick Gold Corporation, Toronto, ON, Canada
[c] Department of Geosciences, Faculty of Sciences and Technologies, University of Kinshasa, Kinshasa XI, Democratic Republic of the Congo
[d] School of Geosciences, University of the Witwatersrand, Johannesburg, South Africa
[e] GFZ German Research Centre for Geosciences, Potsdam, Germany

ARTICLE INFO

Handling Editor: DR Damien Delvaux

Keywords:
Pyrite
Trace elements
Sulfur isotopes
Congo craton
Kibali gold district
Archean orogenic gold deposit

ABSTRACT

The Kibali gold district, located on the Congo Craton, comprises a Neoarchean gold resource exceeding 28.7 Moz. The district is located within a westerly-verging stacked fold-and-thrust belt associated with a compressional tectonic regime active from ca. 2.64–2.60 Ga. Deposits are hosted by a major fault zone that consists of a complex series of smaller thrust faults, shear zones, and folds, which extend over 60 km. Gold deposits are primarily hosted in BIF and clastic sedimentary rocks. The gold and associated sulfides are in veins and disseminated in NE- to NNE-trending ore shoots within the deformed and metamorphosed volcanosedimentary rocks. Pyrite is the dominant sulfide mineral and hosts both solid solution gold and free gold. Because of its strong association with the gold mineralization, our study focusses on unravelling the metallogeny of the area by considering pyrite textural analyses, in situ trace element analyses using Laser Ablation Inductively Coupled Plasma Mass Spectrometry (LA-ICP-MS), and S isotopic composition ($\delta^{34}S$) analyses using Secondary Ion Mass Spectrometry (SIMS).

Eight distinct pyrite types were identified, including microcrystalline sooty (py-0a), small grains (<40 μm) (py-0b), aggregate recrystallized (py-1), core-rich inclusion (py-2), vein-like (py-3), non-zoned (py-4a), oscillatory As-bands zoned (py-4b), and cubic euhedral (py-5) pyrite. The ore-forming processes occurred over a polyphase evolution. Syn-diagenetic pyrite py-0a in volcaniclastic layers of older basin sediments served as the primary repository of Au (15.6 ppm median) with a near-zero $\delta^{34}S$ value. Late diagenetic or early metamorphic pyrite (py-0b) was found in younger basin sediments. Py-1 resulted from solid-state recrystallization of py-0a and py-0b. During the early ore stage, porous py-2 with high Au concentrations (3.1 ppm) and various trace element enrichments precipitated due to fluid-rock interaction. Metal precipitation occurred through sulfidation and carbonation of wall rock with a relatively reduced fluid undergoing ^{34}S-depletion. However, py-3 displayed notable trace element depletion and a complex mineral association. In a second ore stage, py-4a and zoned py-4b deposition occurred, dominated by an over-pressured fluid fracturing brittle rock. Py-4b, rich in Au (5.5 ppm) concentrated in oscillatory zoned As-rich bands, resulted from interactions during pulsed fluid flow. This process involved fluid phase separation, non-equilibrium conditions, ^{32}S-depletion, and precipitation of py-4b with a high $\delta^{34}S$ value (6.4 ‰ mean). Subsequently, pyrite (0–4) generations underwent deformation during a later ductile deformation event, leading to the remobilization and concentration of invisible gold into adjacent gold grains within the high-grade shoot plunging NE. This process involved shearing, boudinaging, and folding ore minerals in tightly folded structures. Late-stage py-5 formed under gold-poor fluid conditions or inefficient gold depositional conditions. Brittle fracturing of these grains later provided local sites for remobilized gold. The study contributes insights into the origin and evolution of gold mineralization in the Kibali gold district, supporting a multistage ore-forming fluid system.

---

* Corresponding author. Barrick Gold Corporation, Toronto, ON, Canada.
** Corresponding author.
E-mail addresses: yannwaku1@gmail.com (Y.W. Mpaka), bvon@sun.ac.za (B.P. Von der Heyden).

https://doi.org/10.1016/j.jafrearsci.2024.105244
Received 13 December 2023; Received in revised form 7 March 2024; Accepted 8 April 2024
Available online 16 April 2024

1. Introduction

The Kibali gold district is located in the northeastern region of the Congo Craton within the Neoarchean Moto Greenstone Belt (Lavreau, 1984; Bird, 2016; Allibone et al., 2020; Mpaka et al., 2023). The district hosts the largest gold deposit of the Congo Craton, named the Karagba-Chauffeur-Durba (KCD) gold deposit (>10 Moz), along with several smaller satellite deposits (<1 Moz) and prospects. The historical mined resources of the district up to 2013 were estimated at 3 Moz (Allibone et al., 2020). Subsequent to this period, the cumulative production from 2013 to 2022, including current resources, is estimated at 25.7 Moz, significantly raising the overall gold resources of the district to over 28.7 Moz Au (Barrick AIF report, 2022). The gold mineralization is generally regarded as being orogenic-type (e.g., Bird, 2016; Allibone et al., 2020), although a recent study suggested that local accumulations of paleoplacer gold may have been overprinted by a later orogenic gold event (Mpaka et al., 2023).

Previous studies (e.g., Bird, 2016; Allibone et al., 2020) have suggested a single ore-forming event over the Kibali district where S, Au and other metals were sourced from the devolatilization process of basaltic/sedimentary rocks buried during the contractional event between 2620 and 2600 Ma. It is noteworthy that the investigation of fluid characteristics within this district is limited, and several deposits remain undocumented in the existing scientific literature. Over 90% of the constituent minerals in the ore are pyrite (FeS_2) (Bird, 2016), which commonly shows an intimate association with gold in the Kibali gold district (Bird, 2016; Allibone et al., 2020). Although categorized as a gangue mineral within most geological contexts, pyrite exhibits a noteworthy propensity for incorporating Au into its structure both through cation exchange type reactions and as small inclusions (e.g., Deditius et al., 2011; Babedi et al., 2022, and references therein). As such, careful investigation of pyrite from the Kibali gold district holds vast potential to help unravel the complex mineralization history of this important gold-producing area.

Studies using pyrite textures and their trace element- and isotope chemistries are increasingly being used to better understand ore deposit formation (e.g., Reich et al., 2005; Large et al., 2009; Barker et al., 2009; Deditius et al., 2011; Reich et al., 2013; Dmitrijeva et al., 2020; Babedi et al., 2022; Wei et al., 2022; Rieger et al., 2023). The usefulness of this mineral as a tool for tracing the evolution of an ore mineralizing system derives from its ubiquity and the fact that it has the capacity to incorporate a wide range of trace elements during crystal growth (Dmitrijeva et al., 2020; Babedi et al., 2022; Rieger et al., 2023). Importantly, trace element uptake into the pyrite structure is governed by the fluid physicochemistry and by the mechanisms of element exchange and adsorption occurring at the fluid–mineral surface (Large et al., 2009; Maslennikov et al., 2009; Keith et al., 2018; Feng et al., 2020; Babedi et al., 2022). For example, in the El Callao gold district, studies on pyrite chemistry have identified two distinct pyrite types (simple-zoned and oscillatory-zoned), revealing a formation process influenced by cyclic shear zone reactivations, pressure variations, and localized fluid circulation (Velásquez et al., 2014). Similarly, Li et al., 2020 combined pyrite trace element measurements with S isotopes to emphasize that the Qiuling gold deposit formed from an ore fluid enriched in As, Au, Cu, and Sb, whereas other metals like Bi, Co, Mn, Ni, and Tl were notably absent. By virtue of being trace elements, i.e., concentrations typically less than 0.1 wt% (Rollinson, 1993), sensitive analytical techniques with low element detection limits and spatial mapping capabilities are needed to understand their distributions in pyrite. In ore deposit studies, multi-trace element analyses of pyrite are now routinely conducted, particularly using Laser-Ablation Inductively Coupled Plasma Mass Spectroscopy (LA-ICP-MS). This is due to the reliable quantitative data that LA-ICP-MS provides, and increasingly also because of its ability to generate two-dimensional element heat maps and depth profile data (e.g., (Large et al., 2007; Sung et al., 2009; Cook et al., 2009; Ciobanu et al., 2009; Velásquez et al., 2014; Fougerouse et al., 2016; Li et al., 2019; Steadman et al., 2021).

This study aims to enhance our understanding of the ore-forming processes and fluid evolution in the Kibali gold district by examining the textures, trace element concentrations, and S isotope signatures of pyrite associated with gold mineralization. We utilized in-situ analytical techniques, including LA-ICP-MS and Secondary Ion Mass Spectrometry (SIMS), to characterize pyrite grains from eight deposits (KCD, Gorumbwa, Kombokolo, Rhino, Agbarabo, Pakaka, Tete Bakangwe, and Kalimva) in the Kibali gold district. The findings from this study hold significant implications for comprehending the large-scale formation of ores in this district. This encompasses understanding the source of fluids flowing through the district and determining the distinct characteristics of each deposit under study. Such insights are essential for resolving the regional and local mechanisms leading to gold precipitation and can be applied to enhance exploration strategies for new deposits in the area.

2. Geological background

2.1. Regional geology

The Neoarchean Kibalian Moto Greenstone Belt (Fig. 1) is located in the northeastern Congo Craton and is primarily composed of variably metamorphosed volcanic and sedimentary rocks. The highest recorded metamorphic grades were experienced towards the eastern part of the belt, where amphibolite facies metamorphism has been documented, while the rest of the belt is dominated by greenschist to upper greenschist facies (Allibone et al., 2020; Bird, 2016), encompassing all deposits studied in this work. For simplicity, we omit the prefix *meta*-in the rest of this text since all rocks have experienced some degree of metamorphism (e.g., *meta*-volcanosedimentary successions will be referred to simply as volcanosedimentary rocks). The basement rocks comprise granite-gneissic rocks (Fig. 1), which surround the Moto Greenstone Belt. To the north lies the Mesoarchean West Nile complex (Lavreau, 1984), for which the age has been recently constrained to ca. 3200 Ma - 2728 Ma, based on U–Pb zircon dating (Turnbull et al., 2021). To the south is the Neoarchean Upper Congo Granite complex (Lavreau, 1984) (Fig. 1), which spans an age range of ca. 2640 to 2530 Ma, as determined by U–Pb zircon dating (Bird, 2016; Allibone et al., 2020; Turnbull et al., 2021).

An ‘old basin’ of predominantly volcanic and volcaniclastic stratigraphy (Fig. 1) was deposited before ca. 2640 Ma (Bird, 2016; Allibone et al., 2020) and was followed by a ‘late basin’ sequence comprising clastic and chemical sedimentary rocks (Fig. 1) which deposited between 2630 and 2625 Ma (Allibone et al., 2020). The central part of the Moto Greenstone Belt, known as the “KZ trend” (Fig. 1b), represents the most gold-endowed zone, hosting numerous deposits and prospects. This trend, situated within the Kibali district, is characterized by a complex series of thrust faults, shear zones and folds extending over many kilometers in strike length (Bird, 2016; Allibone et al., 2020). It coincides with the hydrothermally altered lithostratigraphic suture between the old basin (>2640 Ma) and the young basin (2630-2625 Ma), which was reactivated during the contractional deformation event (Allibone et al., 2020). The early thrust structure initially dips moderately to shallowly east beneath the old basin and is later folded with an NE-to ENE-trending fold axis.

The world-class Karagba-Chauffeur-Durba (KCD) gold deposit and its peripheral gold deposits (Gorumbwa, Sessenge, Kibali south, Kombokolo, Rhino, and Agbarabo) are slightly offset from this trend (Fig. 1b) and contain up to 90% of the current gold resources in the Kibali Gold Mine permit (Allibone et al., 2020; Barrick AIF report, 2022). Most of the remaining gold deposits and prospects in the Kibali gold district occur along or proximal to the KZ trend, including Ikamva, Kalimva, Oere, Kolapi, Mofu, Mengu Hill, Megi-Sayi-Marakeke, Pamao, Tete Bakangwe, Pakaka, and Aerodrome deposits in the northern branch (Fig. 1). The southern branch of the KZ trend contains several Au prospects including Aindi-Watsa, Zambula, Zakitoko and Zembe (Bird, 2016; Allibone et al., 2020).

2.2. Deposit geology

The deposits considered in this study include a group of selected deposits within the KCD area (KCD, Agbarabo, Rhino, Kombokolo, and

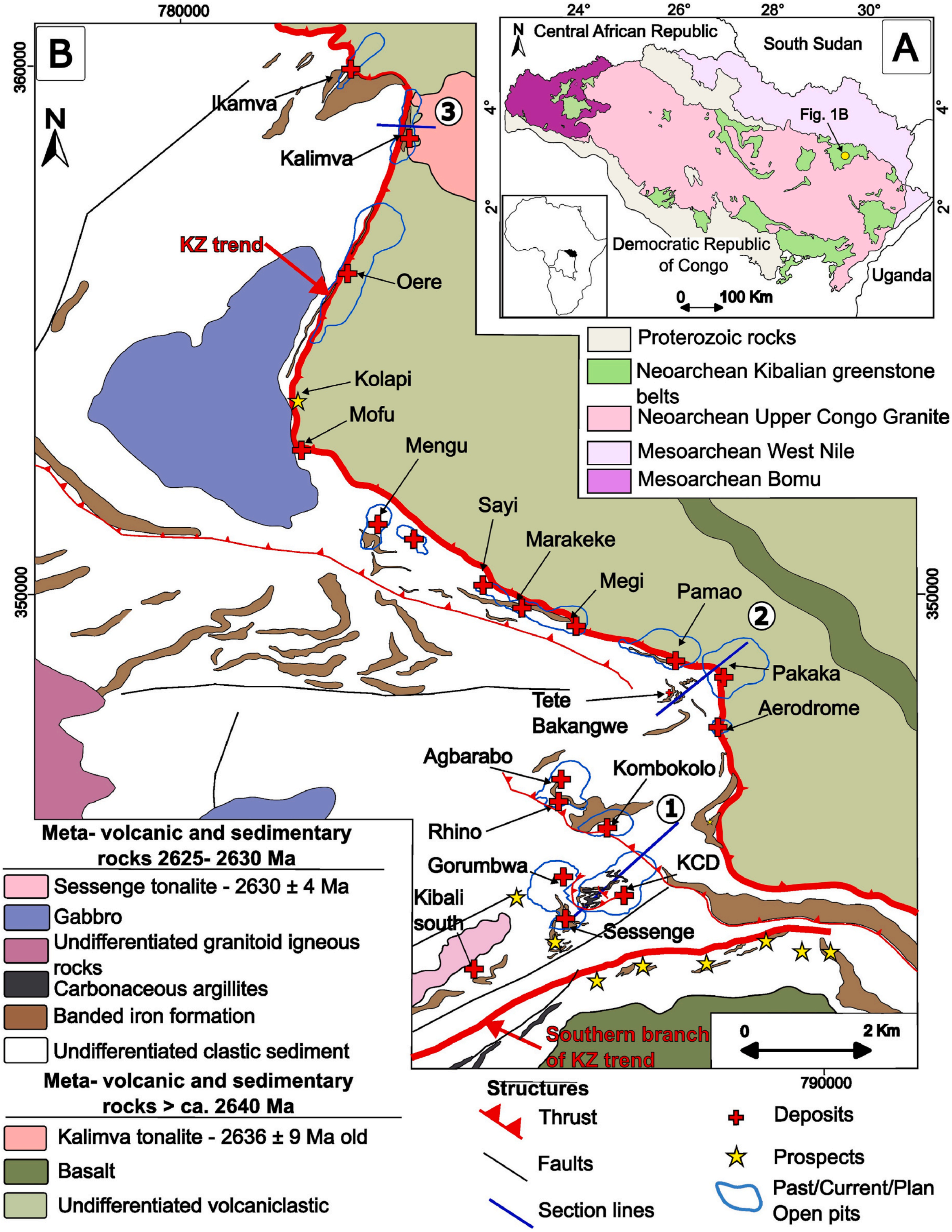

Fig. 1. Geological map of the Kibali gold district in the Moto greenstone belt. A. Summary geologic map of the northeastern Congolese part of the Congo Craton. B. Geological map of the Kibali gold district with earlier volcaniclastic stages (>2640 Ma) lying east of the KZ trend. The later series (2630–2625 Ma) is situated directly west of the northern branch of the KZ trend and is mainly composed of clastic and chemical metasediments. Section line 1 drawn on the KCD deposit is shown in Fig. 2, section line 2 drawn on the Pakaka and Tete Bakangwe deposit is shown in Fig. 3, and section line 3 drawn on the Kalimva deposit is shown in Fig. 4. Modified after Bird (2016), Allibone et al. (2020), and Mpaka et al. (2023).

Gorumbwa) and deposits located further north along the KZ trend (Pakaka, Tete Bakangwe, and Kalimva). Deposits within the KCD area form a tight cluster and share geological similarities. Pakaka and Kalimva are located close to, or at, the contact between the old and late basins, manifested by a basin bounding structure. Tete Bakangwe is slightly offset from this boundary and shows many geological similarities with the cluster of deposits in the KCD area (Fig. 1).

2.2.1. KCD area

The KCD area (Fig. 1; Fig. 2) comprises late basin lithostratigraphy dominated by clastic and chemical sedimentary rocks deposited between 2630 and 2625 Ma (Allibone et al., 2020). The lithotypes in this area are subdivided into two distinct rock packages metamorphosed under greenschist facies (Allibone et al., 2020; Mpaka et al., 2023). The first is known as the Kanga Sud package, located in the hanging wall section. This package is primarily characterized by fine-grained rocks, including interbedded carbonaceous shale and siltstone, with minor occurrences of sandstone and conglomerates. It is also intruded by diorite dykes, as detailed in Mpaka et al. (2023). Additionally, a BIF/chert unit is found near the top, close to the contact with the older volcaniclastic sequence, and is locally mineralized. Another BIF unit is situated at the bottom of this domain, in contact with the footwall package (Fig. 2). Conversely, the footwall package is predominantly composed of sandstone, along with mono- to polymictic conglomerates interbedded with BIF/chert and carbonaceous argillite. Moreover, there are minor occurrences of felsic to mafic volcanic rocks and intrusive rocks within this package (Fig. 2). The footwall package exhibits a higher degree of folding and shearing compared to the hanging wall package and is the primary host for KCD gold mineralization (Fig. 2) (Allibone et al., 2020; Bird, 2016; Mpaka et al., 2023).

Hydrothermal alteration in the KCD area has been divided into two main stages (Bird, 2016; Allibone et al., 2020). The first barren stage, a widespread pre-ore event, is characterized by quartz-carbonate-sericite alteration and occurred during the tight-to-isoclinal folding and shearing event, impacting the earlier regional metamorphic assemblage (Allibone et al., 2020). The second stage, representing the main ore-forming event, is characterized by a quartz-carbonate-sericite-sulfide-gold alteration assemblage and is texturally destructive. This alteration assemblage is present locally in the gold deposits and elsewhere along the KZ trend, including locations lacking economically significant Au mineralization (Allibone et al., 2020). Although a recent study has highlighted the importance of pre-orogenic gold within the conglomerates (Mpaka et al., 2023), the primary exploration target are the structurally controlled quartz-carbonate-sericite-sulfide-gold alteration zones (Allibone et al., 2020). These structures cross-cut sheared siliclastic rocks, BIF, and chert units wherein the mineralization manifests as fine disseminations or cm to mm-sized sulfide veins (Allibone et al., 2020). Notable Au endowments are found where shear zones intersect reactive BIF layers as the gold mineralization gently plunging towards the NE and, in places, following the fold axes and/or limbs (Bird, 2016; Allibone et al., 2020).

2.2.2. Pakaka – Tete Bakangwe deposits

Pakaka and Tete Bakangwe deposits (Fig. 1b; Fig. 3) are located approximately 5 km northeast of the KCD deposit (Fig. 1b). The Pakaka deposit (Fig. 1; Fig. 3) is situated along the boundary between the older eastern basin (>2640 Ma) and the later basin (2630-2625 Ma), while the Tete Bakangwe is located just below the Pakaka deposit and is entirely within the later basin (Allibone et al., 2020). The rock types of the hanging wall sequence (old basin) primarily consist of sub-greenschist to upper greenschist facies metamorphosed and altered basalts, dacitic-rhyolitic volcaniclastic rocks, carbonaceous shale, crystal-ash tuffs, and minor siltstones and banded iron formations (BIF) (Bird, 2016; Allibone et al., 2020). On the other hand, the footwall rock package (late basin) mainly comprises immature gritstone, sandstone, minor pebbly gritstone, and BIF (Bird, 2016; Allibone et al., 2020).

At Pakaka (Fig. 3), gold mineralization occurs within the sheared lithostratigraphic boundary. It is associated with a wall rock alteration signature comprising predominantly chlorite and quartz, along with Fe-carbonate, pyrrhotite, ± pyrite, and ± arsenopyrite (up to 20% of total sulfide content) (Bird, 2016; Allibone et al., 2020). In contrast, in Tete Bakangwe (which shares similarity with the KCD style), fold structures with BIF host rocks are considered a dominant control on the siting of the Au mineralization (Bird, 2016; Allibone et al., 2020). The alteration

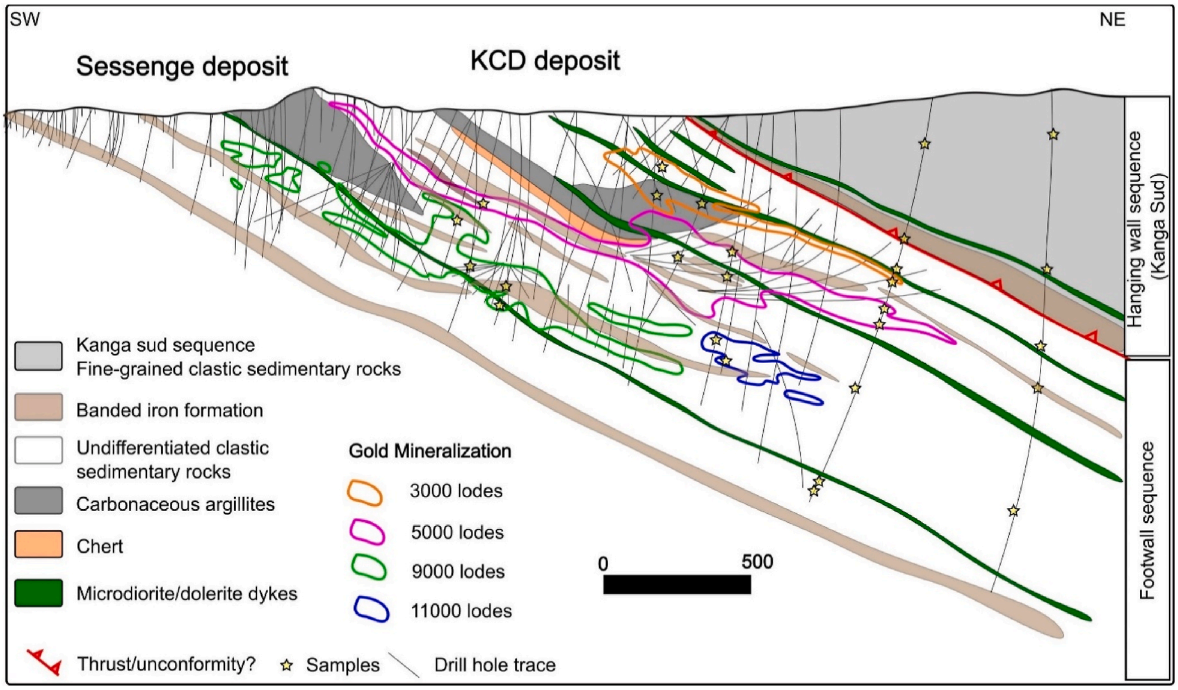

Fig. 2. Crossing strike sections showing lithological sequence and mineralization of the KCD deposit with different lodes series of gold mineralization including 3000, 5000, 9000, and 11000 lodes.

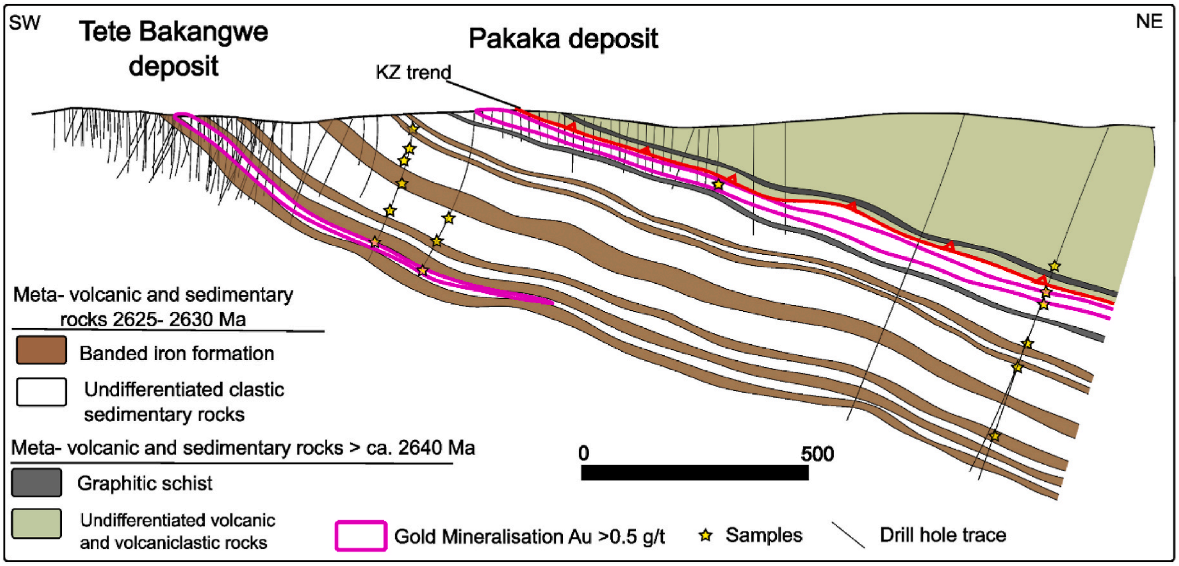

Fig. 3. Crossing strike sections showing lithological sequence and mineralization of the Pakaka and Tete Bakangwe deposits.

is dominated by Fe-carbonate, quartz, sericite, chlorite, pyrite, and pyrrhotite, with rare occurrences of arsenopyrite and chalcopyrite (Bird, 2016). The general trend of gold mineralization in Pakaka and Tete Bakangwe strikes NW-SE (parallel with the mineral foliation), and ore shoots typically exhibit a shallow NE plunge (Allibone et al., 2020, Fig. 3).

2.2.3. Kalimva deposit

The Kalimva deposit (Fig. 1b; Fig. 4) was first discovered by the Belgian explorationists in the early 1950s, and mining commenced as an open-pit operation during the same year (Barrick report, 2022). This deposit is located approximately 14 km northwestern from the KCD deposit (Fig. 1b) and along the lithostratigraphic boundary between the old and late basins (Fig. 4). Its stratigraphic position is similar to that of Pakaka and it was metamorphosed at lower to upper greenschist facies metamorphism (Fig. 1b; Fig. 4), with volcanogenic rock types in the hanging wall sequence and siliciclastic sedimentary rocks dominating in the footwall sequence (Fig. 1b; Fig. 4). However, unlike at Pakaka, Kalimva is situated close to an intrusive body (tonalite dated at 2636 ± 9 Ma; Bird, 2016, U–Pb zircon, LA-ICP-MS), and the BIF unit is interbedded in the old basin volcaniclastic series (Fig. 4). In addition, the ore mineralization strikes NNE-SSW with an NNE plunge (Allibone et al., 2020). Early alteration is indicated by a quartz, sericite ± carbonate mineral paragenesis, later overprinted by pervasive chlorite with penetrative chlorite shear foliation and occasional pyrite and pyrrhotite veins. Late-stage alteration involves phlogopite with randomly oriented

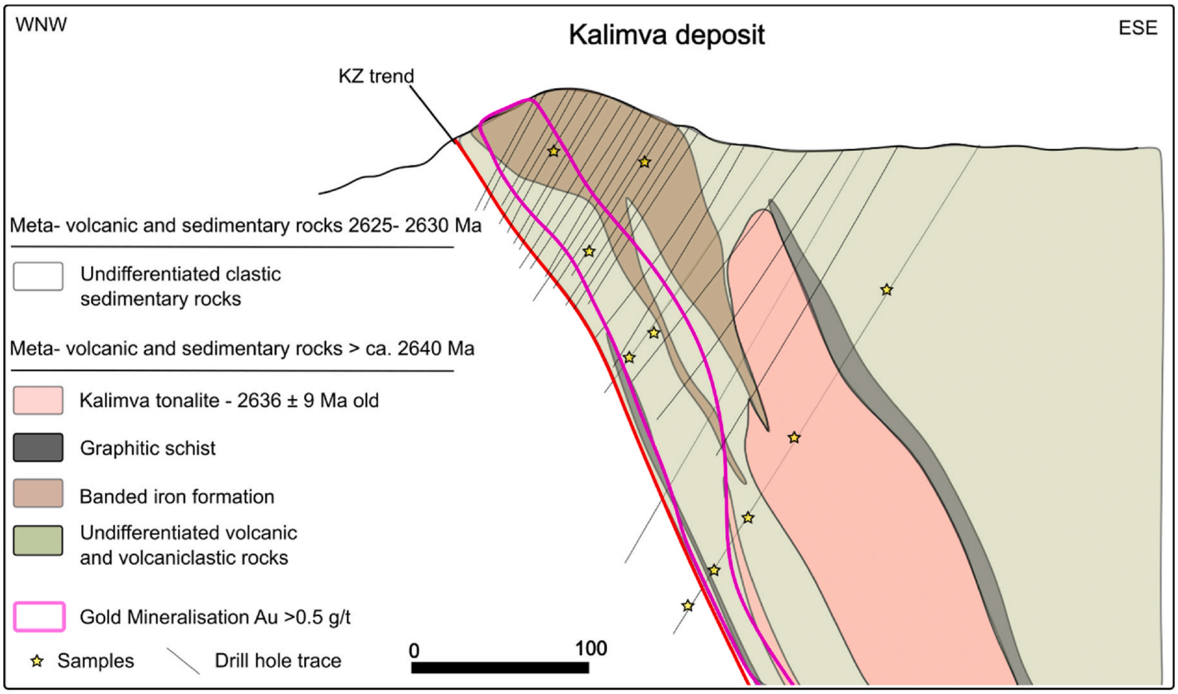

Fig. 4. Crossing strike sections showing lithological sequence and mineralization of the Kalimva deposit.

minerals and carbonate veinlets. The absence of texturally destructive quartz-carbonate-sulfide-gold alteration distinguishes Kalimva from other gold deposits in the Kibali district (Allibone et al., 2020). Gold mineralization is generally associated with disseminated or stringer pyrite aggregates along chlorite foliation within shear zones, with pyrrhotite predating mineralization. Arsenopyrite and chalcopyrite are occasionally present in the sulfide mineralogy (Allibone et al., 2020).

3. Methods

3.1. Sampling and optical microscopy

A total of 91 samples were collected from a set of 26 diamond drill holes to ensure an as representative analysis as possible. From these samples, 90 thin sections and 101 polished sections encompassing various rock types were prepared. To identify and prioritize sections for further analysis, 19 polished sections were carefully selected based on their distinct petrographic characteristics (Table 1). As with any pyrite microtexture study, the extrapolation of these micrometer-scale insights to the regional scale must be treated cautiously, and we present our interpretations in a moderated fashion and as a contribution that will serve as a benchmark for further detailed works. The selected polished sections were used for in situ analysis of pyrite trace elements. In addition, six polished sections were selected explicitly for S isotope analysis based on their representativeness of the different generations of pyrite (Table 1).

3.2. Scanning electron microscope (SEM)

The SEM analysis was conducted on carbon-coated mounts using a Zeiss EVO MA15VP coupled with an OXFORD INCA Electron Dispersive Spectrometer (SEM-EDS) and with Wavelength Dispersive Spectrometer (WDS) at the Central Analytical Facility of Stellenbosch University, South Africa. The equipment was used in Backscatter Electron Imaging (BSE) at a free working distance of 8.5 mm, at a 20 kV accelerating voltage, with high magnifications exceeding 1000x, and at a current of about 19.5 nA. Different X-ray lines were used to reduce spectrum overlaps, and the international mineral standards provided by Astimex Scientific Limited (MINM25-53 Mineral Mount Serial No: 03–040 and METM25-44 + FC Metal Standard Mount Serial No: 50–010) were used for spot calibration. The detection limit for EDS is ca. 0.1 wt%, while WDS is ca. 0.01 wt%.

3.3. LA-ICP-MS (in situ trace element analyses)

LA-ICP-MS in the Central Analytical Facility (Stellenbosch University, South Africa) performed trace element analyses on pyrite minerals. The Agilent 8800 QQQ ICP-MS equipment was linked with a Resolution 193 nm Excimer laser from Applied Spectra. The sample cell containing the material was filled with helium (He). After the laser ablation, the material was combined with argon and a tiny quantity of nitrogen before being delivered to the ICP-MS. The initial step involved optimizing laser gas flow and ICP-MS settings to ensure maximum sensitivity and minimal oxide ratios (<0.4%) during the laser ablation process on NIST612. Then, based on the sensitivity or potential interferences to be eliminated, all the analytes were measured using oxygen as the reactive cell gas at a flow of 0.68 ml/min, either on mass or mass-shifted (analyte mass + 16). The spot studies were conducted at 3 J/cm^2 fluences and 6 Hz frequency with a 20–30 μm beam size.

For LA-ICP-MS analysis, monitored isotopes were ^{34}S with limit of detection (LOD):0.1 (%), ^{47}Ti (LOD: 0.03 ppm), ^{51}V (LOD: 0.01 ppm), ^{52}Cr (LOD: 0.25 ppm), ^{55}Mn (LOD: 0.08 ppm), ^{57}Fe, ^{59}Co (LOD: 0.03 ppm), ^{60}Ni (LOD: 0.15 ppm), ^{63}Cu (LOD: 0.11 ppm), ^{66}Zn (LOD: 0.19 ppm), ^{69}Ga, ^{71}Ga, ^{72}Ge (LOD: 0.03 ppm), ^{75}As (LOD: 0.10 ppm), ^{77}Se (LOD: 0.41 ppm), ^{95}Mo (LOD: 0.002 ppm), ^{107}Ag (LOD: 0.03 ppm), ^{111}Cd (LOD: 0.01 ppm), ^{115}In (LOD: 0.003 ppm), ^{118}Sn (LOD: 0.02 ppm), ^{121}Sb (LOD: 0.01 ppm), ^{128}Te (LOD: 0.04 ppm), ^{133}Cs (LOD: 0.001 ppm), ^{139}La (LOD: 0.001 ppm), ^{157}Gd (LOD: 0.001 ppm), ^{182}W (0.00003 ppm), ^{197}Au (LOD: 0.02 ppm), ^{202}Hg (LOD: 0.62 ppm), ^{205}Tl (LOD: 0.03 ppm), ^{208}Pb (LOD: 0.02 ppm) and ^{209}Bi (LOD: 0.01 ppm). The internal standard element (ISTD) ^{57}Fe was chosen. The standard deviations were calculated by utilizing certified trace element values from certified materials (BHVO-2G and Po 725) in comparison to measured values obtained during the analyzed session. The results indicate a generally low standard deviation (less than 20), except for Ti (around 600) and Mn (approximately 70). Comprehensive details are provided in Appendix A.5. The pyrite grain's elemental maps were generated using LA-ICP-MS with a spot size of 15 μm and a scan speed of 10 μm/s. The grid tool in

Table 1
Summary of samples selected in the Kibali gold district for LA-ICP-MS and SIMS analyses, showing the number of analyses per pyrite type for each method.

Deposits	Samples	Rock types	Au grade (g/t)	LA-ICP-MS (spot)[a]								LA-ICP-MS (spot)	LA-ICP-MS (map)	SIMS (spot)
				Py-0a	Py-0b	Py-1	Py-2	Py-3	Py-4a	Py-4b	Py-5	All pyrite		
KCD	YWK002	BIF	No assay		15		3		5	2		27		
	YWK007	Conglomerate	48.3			3	5		1	9		27	1	10
	YWK009	BIF	11.5		2		18		3		1	27		10
	YWK012	BIF	0.09			17	2		1	1		24	1	11
	YWK017	Conglomerate	24.5		2		10		1	6		23		
	YWK025	Conglomerate	16.1				1	16				17		10
	YWK087	Breccia	7.06				11		4	3		24		
	YWK091	Conglomerate	33.3		1	9				1	1	18	2	
Kombokolo	YWK078	BIF	0.01		8		4		2	1	1	19		
	YWK079	BIF	40.2		5		5		3		4	21		
Gorumbwa	YWK080	Conglomerate	20.1						2	2		7		
Agbarabo	YWK086	Conglomerate	129		1	8	2		5		5	28	1	
Pakaka	YWK070	Basalt	0.005			1					10	13		
Tete-Bakangwe	YWK059	Volcaniclastic	1.52		1		2		2		1	6		
	YWK061	BIF	6.28				1				1	3	1	10
	YWK068	BIF	4.11		6	2	5		9	2	4	39		
Kalimva	YWK036	Volcaniclastic	2.41				7		6	4	1	22		
	YWK040	Mafic volcaniclastic	0.03						3		5	12		
	YWK041	Volcaniclastic	20.2	7		8	5	1		4		33	1	9
Total	19			7	49	39	81	17	47	35	35	390	7	60

[a] *LA-ICP-MS spot dataset of pyrite selected after pre-processing detailed in* Mpaka and von der Heyden (2024, *this issue).*

ioGAS software was used to analyze and interpolate the raw data that was produced. The US Geological Survey's matrix-matched standard MASS-1 was employed. The LA-ICP-MS data reduction software tool LADR from Norris Scientific was used to process the data Norris and Danyushevsky, 2018). Final concentrations were estimated using a normalization method that reduced element contributions to 99.9%, with the resulting total signal being proportional to the amount of material ablated (Leach and Hieftje, 2000). Reference values from the GEOREM database for NIST612, MASS-1 sulfide (Jochum et al., 2005, 2016). The subsequent sections will present the concentrations of trace elements as (median in ppm; standard deviation).

3.4. In situ S isotope analyses (SIMS)

The S isotope composition ($\delta^{34}S$) analysis was conducted using the University of the Witwatersrand virtual SIMS facility. This facility is connected via an internet-based link to the Cameca 1280-HR instrument located at the Helmholtz Zentrum Potsdam, Germany. Different generations of pyrite were carefully selected in six polished sections after petrography and LA-ICP-MS trace element studies to identify $\delta^{34}S$ in pyrite analysis spots.

Before analysis, the samples were cleaned and sputter coated with a 35 nm, high-purity gold film. The SIMS analyses in Potsdam employed a primary ion beam of $^{133}Cs^{+}$ at an intensity of approximately 1 nA with a beam size of 5 μm. Negative secondary ions were obtained through a −10 kV potential applied to the sample holder, and charge compensation was achieved through low-energy electron flooding. The instrument was worked in FC-FC multi-collection mode, with a mass resolving power approximately equal to $M/\Delta M \approx 5000$ (at 10% peak height). This level of resolution effectively distinguished between ^{32}S and ^{34}S using the L′2 trolley alongside FC2 for the respective S isotopes.

The data were filtered at the 3-sigma level, and the average pressure in the sample chamber was 2.3×10^{-6} Pa. The sample mounts were periodically replaced with a separate mount containing the Balmat pyrite reference material, designed as a geochemical reference material for S isotope ratio determinations. During a three-day session, the Balmat pyrite (which has a $\delta^{34}S_{VCDT}$ value of 15.1 ‰ (Crowe and Vaughan, 1996)) was evaluated 56 times, resulting in daily repeatabilities of 0.039, 0.080, and 0.084 ‰, respectively. The zero point on the $\delta^{34}S_{VCDT}$ scale ($^{34}S/^{32}S = 0.044163$; Ding et al., 2001) was then used to determine the mean Instrumental Mass Fractionation (IMF) of the reference material: 1.0038, which was then utilized to correct the measured $^{34}S/^{32}S$ ratio, from which the delta value for the unknowns is calculated.

4. Results

4.1. Pyrite occurrence and texture

Pyrite is the most widespread sulfide occurring in the Kibali gold district, where, in some places within the ore zone, it constitutes up to 90% of the total ore mineral assemblage. It occurs in different manifestations, including as isolated grains or as vein minerals within cm-scale quartz-carbonate veinlets (Fig. 5a–c, d), disseminated within the altered wall rocks, and along the planar features such as bedding planes and shear foliations (Fig. 5b and c). Among the various samples evaluated, the pyrite is variably associated with different sulfides, such as pyrrhotite, arsenopyrite, chalcopyrite, Fe-oxide minerals, phosphates, and sulfosalts.

Based on a dimensionality reduction method for trace elements described in an accompanying paper (Mpaka and von der Heyden, 2024 this issue), combined with observations of occurrence, grain size, morphology, and detailed textural analyses, a total of eight pyrite types (categorized into five broad groupings) were identified. They are defined here in their paragenetic sequence and are illustrated in Fig. 7.

- **Pyrite-0a (py-0a):** Microcrystalline (<20 μm across) sooty grains, subhedral to euhedral form. Framboid aggregates can reach up to 100 μm diameter (Fig. 6a; Fig. 7a). The py-0a occurs in the sandy volcaniclastic interbeds within volcanic rock-types from Kalimva deposit (Figs. 1 and 2b). These pyrites are disseminated within the silicate matrix and exhibit a textural similarity to the framboidal and sooty pyrite described by Large et al. (2007) and George et al. (2018).
- **Pyrite-0b (py-0b):** Euhedral to subhedral habit, these pyrites are characterized by small sizes, typically less than 40 μm (Fig. 6b; Fig. 7a). Py-0b is commonly found along phyllosilicate or magnetite mineral foliation or dispersed within the gangue, in places, surrounded by other types of pyrite. Some py-0b grains are inclusions within oxide minerals such as magnetite, ilmenite, and rutile.
- **Pyrite-1 (py-1)**: Appearing as euhedral to subhedral grains, py-1 occurs either isolated or as aggregates originating from py-0a or py-0b, with sizes ranging from 50 μm to 1 mm (Fig. 6b and c; Fig. 7a) (e.g., Zhao et al., 2021). Py-1 can also be rimmed by py-2 (Fig. 6c).
- **Pyrite-2 (py-2):** Typically appears as subhedral core pyrite (Fig. 6b, c, d; Fig. 7a) with numerous tiny inclusions of carbonate, gold, sulfide, silicate, oxide, phosphate (monazite, apatite, and xenotime), sulfate (baryte), tungstate (scheelite), and sulfosalt. This type of pyrite is widely distributed in most of the district's samples (both ore and barren).
- **Pyrite-3 (py-3)**: Anhedral crystal form occurs like a massive pyrite-veinlet and, in places, replaces pyrrhotite (Fig. 6e; Fig. 7a). This pyrite is commonly partly annealed and displays skeletal forms and/or clustered intergrowths with marcasite. It is commonly rimmed by the siderite. It is mainly observed in the up-plunge portions of the 3000 lode ore zone at the KCD deposit. Pyrite-3 commonly contains tiny random inclusions bearing gold, chalcopyrite, pyrrhotite, and sulfosalts (e.g., tennantite, tetrahedrite, Ni-rich cobaltite).
- **Pyrite-4:** This type typically occurs as a rim around py-2 and is characterized by having fewer mineral inclusions. There are two subtypes, including **py-4a** (Fig. 6c; Fig. 7a), which is non-zoned and more homogeneous, and **py-4b** (Fig. 6d; Fig. 7a), characterized by oscillatory As-rich bands, visible under backscattered images in SEM.
- **Pyrite-5 (py-5):** Characterized by large pyrite grains from 200 μm to >2 mm. The pyrite grain habit ranges from euhedral to subhedral, typically homogeneous or with fewer inclusions (Fig. 6f; Fig. 7a). In places, it occurs as isolated grains in the matrix or within quartz veins that intersect the foliation. In some cases, it preserved the fabric of the surrounding material as it grew, including evidence of multiple phases of deformation.

4.2. Pyrite in relation to deformation

Given the complex deformation history in our study area, elucidating the relationship of pyrite to the multiple deformations presents a significant challenge. It is essential to note that delving into the deeper intricacies of deformation history is not the primary focus of this study. However, in this section, we aim to establish a basic relationship between the defined pyrite generations and various structural features through macro- and microscopic observations. Fig. 8 illustrates different deformation features, encompassing ductile aspects such as shearing, mineral foliation, and folding, as well as brittle features like faulting and fracturing.

The generation of pyrites py-0a and py-1 are associated with elongated pyrrhotite and are aligned along the penetrative chlorite foliation, exhibiting a sheared, sigmoid shape (Fig. 8a and b). Additionally, textural analysis suggests the replacement of py-0a by pyrrhotite, as the latter contains numerous inclusions of this pyrite type (Fig. 8a and b). On the other hand, Fig. 8c and d illustrate the cross-cutting and shearing of the early mineralized pyrite (2, 4)-quartz veinlets (S_n) by the penetrative sericite foliation (S_{n+1}). The 'n' annotation with 'S' (foliation) indicates these observations were not integrated into the broader

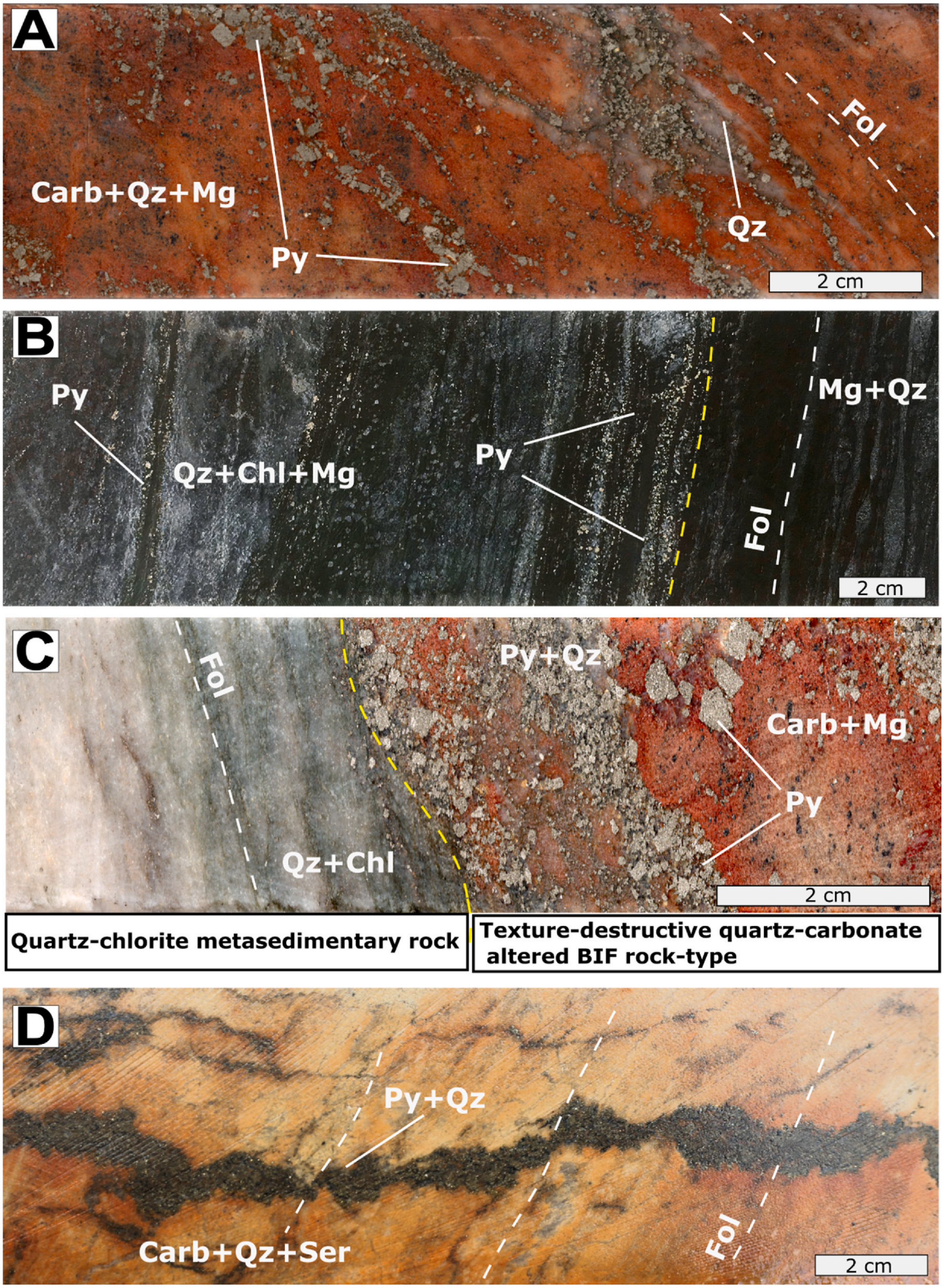

Fig. 5. Various macroscopic features of pyrite occurrences in the Kibali Gold district are illustrated through hand specimens from KCD (A and D), Kalimva (B) and Kombokolo (C). **A.** Pyrite veins and disseminated occurrences associated with veinlets of quartz veins along the anastomosed plane, subparallel to the mineral foliation (dashed white line) within a texture-destructive quartz-carbonate alteration with magnetite relics of the ironstone protolith. **B.** Sheared BIF altered by pervasive quartz and chlorite, with pyrite along the mineral foliation (dashed white line) increasing in proportion along the contact between the altered and less-altered zones. **C.** Disseminated and pyrite veins with different sizes occurring within the texture-destructive quartz-carbonate alteration with magnetite relics of the ironstone protolith, while the quartz-chlorite metasedimentary rock remains barren (contact illustrated in yellow dashed line). **D.** Pyrite-quartz veins occurring within the metasedimentary rock altered by quartz, carbonate, and sericite. The quartz-pyrite veins are crosscut by sheared mineral foliation (white dashed line). Abbreviations: Py: pyrite; Chl: chlorite; Mg: magnetite; Carb: carbonate; Qz: quartz; Ser: sericite; Fol: foliation.

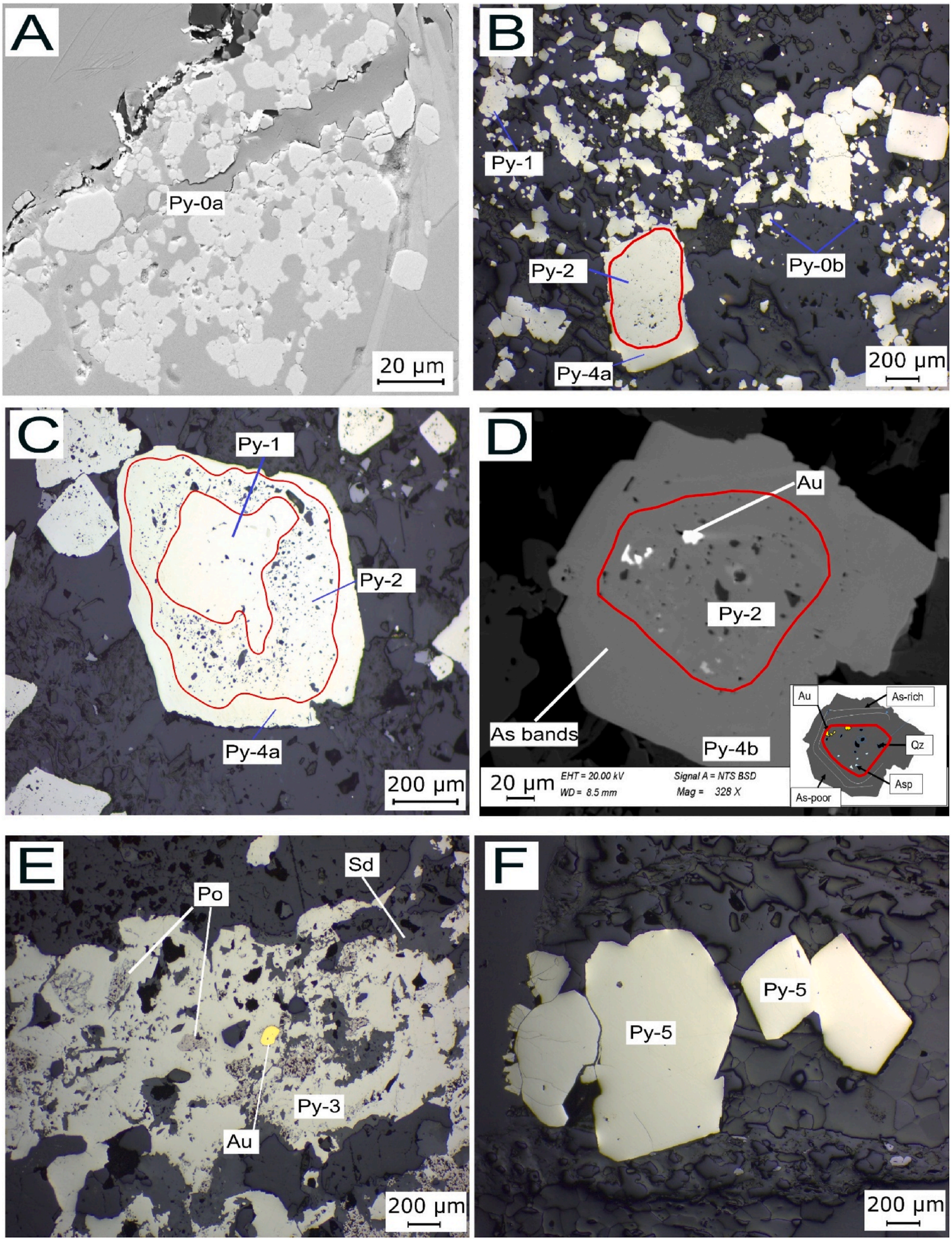

Fig. 6. Reflected light and backscattered electron photomicrographs from the Kibali Gold district show different textural characteristics of various pyrite types. **A.** Fine microcrystalline grains of pyrite, forming a subhedral to anhedral aggregate (py-0a) from Kalimva deposit, collected in sample YWK041 (volcaniclastic lithotype). **B.** Disseminated fine-grained py-0b tends to aggregate and form py-1 adjacent to the coarse-grained core (py-2) and rim (py-4a) observed within the sample YWK078 from the Kombokolo deposit (conglomerate lithotype). **C.** Subhedral pyrite grain showing core-rim texture with a core containing less inclusion (py-1) rimmed by rich-inclusion pyrite (py-2) and surrounded by pyrite with less-inclusion (py-4a), observed within the conglomerate (YWK091) from the KCD deposit. **D.** Subhedral core-rim pyrite with py-2 in the core and As-rich bands zonation (py-4b) from Tete Bakangwe deposit collected from sample YWK068 (BIF). **E.** Irregular pyrite veinlet (py-3) replacing pyrrhotite and replaced by siderite collected from sample YWK025 (conglomerate) within the KCD deposit. Pyrite contains one grain of enclosed gold. **F.** Coarse euhedral to subhedral inclusion-poor pyrite (py-5) grains within sample YWK070 collected in the Pakaka deposit. Abbreviations: Py: pyrite; Sd: siderite; Po: pyrrhotite; Qz: quartz; Asp: arsenopyrite; Au: gold.

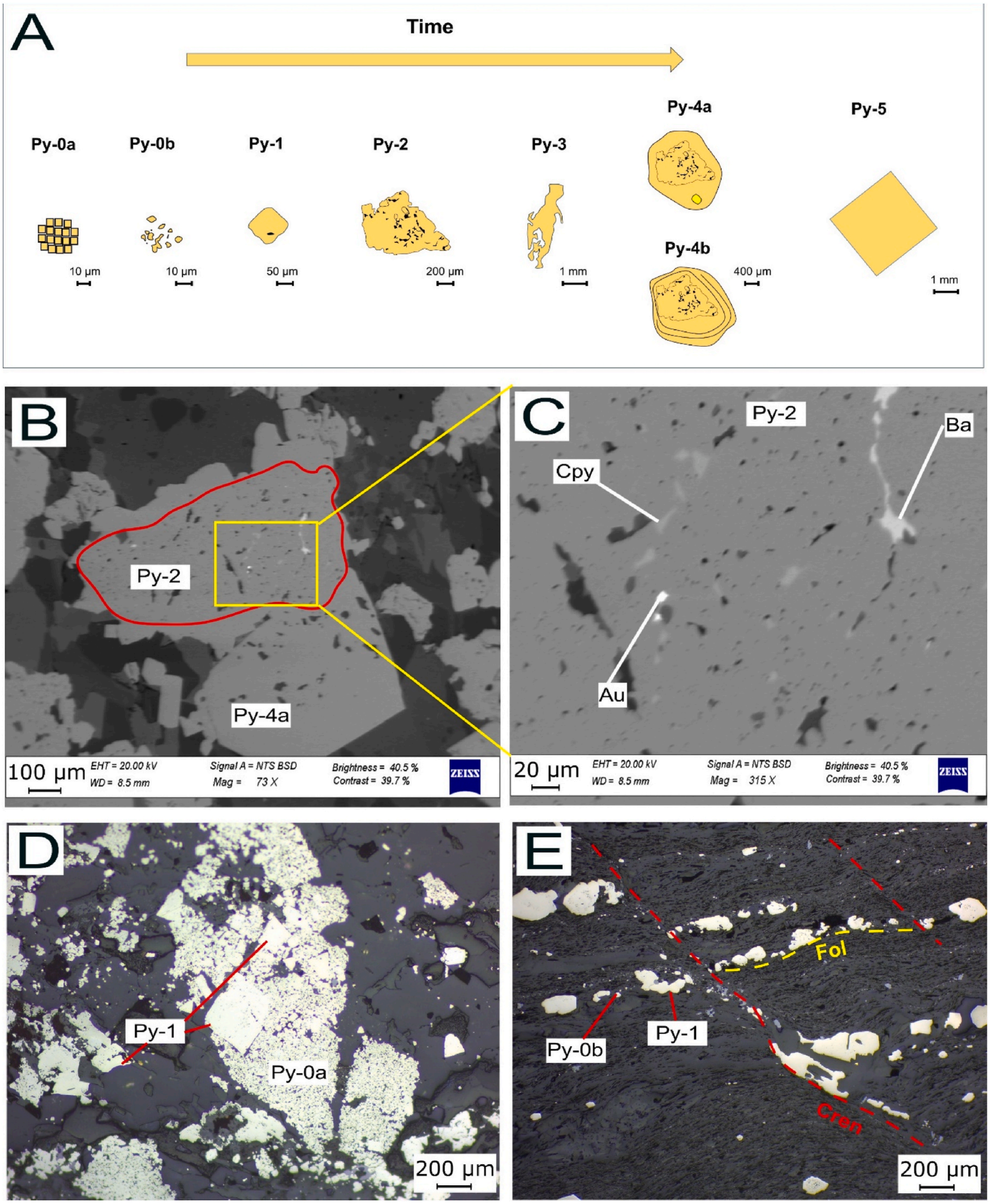

Fig. 7. **A.** Sketch illustrates the paragenetic sequence of different pyrite types over time during the evolution of the Kibali Gold District. **B** and **C**. Backscattered electron photomicrographs illustrating py-2 (core) and py-4a (rim) with anhedral barite (Ba) adjacent to gold (Au) and chalcopyrite (Cpy) minerals precipitated within py-2. **D** and **E**. Reflected light photomicrographs show the formation of: (D) py-1 by the aggregation of py-0a from a sample collected in the Kalimva deposit within the metamorphosed volcaniclastic lithotype (YWK041) and (E) the formation of py-1 by the aggregation of py-0b from a sample collected in the Agbarabo deposit (YWK086) within the metamorphosed sedimentary lithotype affected by foliation and crenulation.

regional deformation history, as their correlation with the tectonic evolution remains unexplored. This penetrative foliation boudinaged, dismembered (Fig. 8c and d) and folded the pyrite (2, 4)-quartz veinlets (Fig. 8c and d). Fig. 8g, h, and i also illustrate these features of sheared and folded quartz-pyrite veins. Fig. 8e exemplifies the elongation of the pyrite (4b) within a sheared metaconglomerate with sericite-quartz-rich groundmass. The pyrite and gold grains (Fig. 8e) are preferentially oriented along the sericite-dominant penetrative foliation fabric, where in some places, gold grains occur as a pressure shadow of pyrite grains. Furthermore, the sheared crenulation fabric (S_{n+2}) deforms these generations from py-0 to py-4 (Fig. 7e). Fig. 8f shows fractured pyrite 5 filled by a Au vein. In some places, these fractures are associated with galena, chalcopyrite, and gold grains.

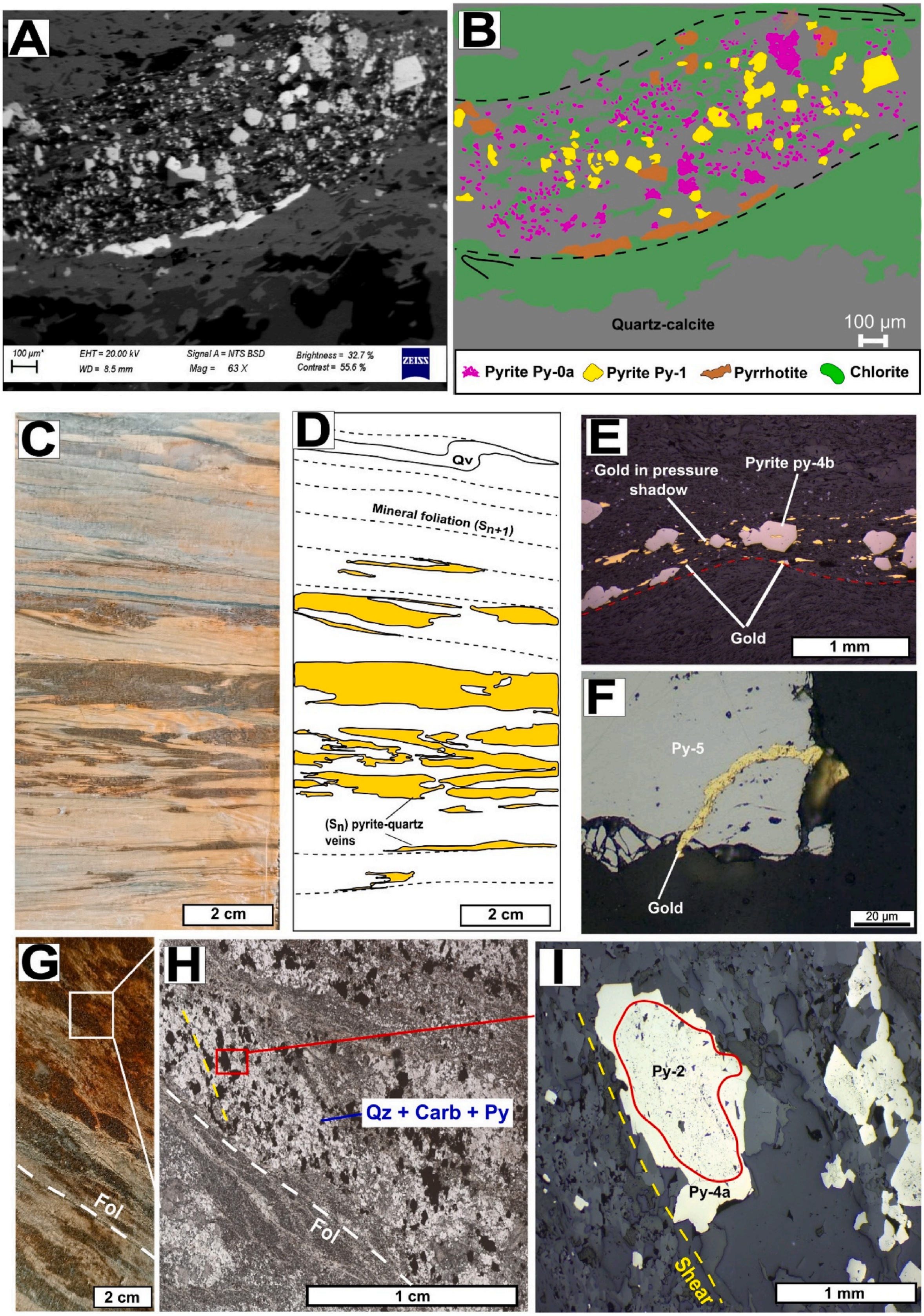

(caption on next page)

Fig. 8. Representative evidence of deformed sulfide under both ductile and brittle regimes in the Kibali Gold District. **A** and **B.** Backscattered photomicrograph and sketch from Kalimva deposit collected in sample YWK041 (volcaniclastic), respectively, illustrating a sheared mineral assemblage of pyrite (py-0a transformed by aggregate into py-1) in association with pyrrhotite. The latter mineral is strongly stretched in contact with a large zone of chlorite-rich minerals. The groundmass consists of quartz-calcite and chlorite affected by dextral shearing. **C** and **D.** Hand specimen of strongly deformed metasandstone displaying early auriferous quartz-pyrite veinlets (S_n) tightly folded by the sericite-chlorite foliation (S_{n+1}), which is subparallel to the axial plane. The rock type is altered by Fe-carbonate and collected from the KCD deposit. **E.** Reflected light photomicrograph of deformed metaconglomerate rock type (Agbarabo deposit) exhibiting both the deformation of gold grains and pyrite (py-4b) along the sericite-rich foliation (red line). Gold grains are observed in some places, acting as a pressure shadow mineral of pyrite. **F.** Reflected light photomicrograph of fractured pyrite (py-5) hosting a gold vein (KCD deposit). **G, H,** and **I.** Hand specimen, scanned thin section, and reflected light photomicrograph, respectively, of a strongly deformed conglomerate displaying sheared, folded, and boudinaged quartz-pyrite veins (py-2 and py-4a along shear in the yellow line) along the sericite-rich foliation (white line) from KCD deposit. Abbreviations: Py: pyrite; Qv: quartz vein; Carb: carbonate; Fol: foliation; Qz: quartz.

4.3. LA-ICP-MS trace element spot analyses

The chemical trace element characteristics of the pyrite grains evaluated from the various deposits in the Kibali gold district are provided in Table 2, Fig. 9, and Appendix A.1. It should be noted that a limited dataset is available for the Gorumbwa and Pakaka deposits, and they are thus not included here in comparison with the other deposits. Additionally, the dataset for each pyrite generation is also limited. Nonetheless, an overall comparison indicates that most trace elements exhibit substantially higher concentrations in KCD and Kalimva pyrites, i.e., more than one order of magnitude, compared to the other deposits in the Kibali gold district (Table 2).

In the context of pyrite types within the district, py-0a (Fig. 9, Table 2) is exclusively identified in the Kalimva sample (YWK041). This pyrite type demonstrates notable enrichment in Au along with chalcophile elements such as As, Sb, Pb, Hg, Bi, Cd, Mo and Sn, as well as base metals like Cu and Ni (Fig. 9). These elements exhibit elevated median values with low standard deviations including Au (15.6 ppm; 1.6), As (8895.5 ppm; 717.8), Bi (54.5 ppm; 10.3), Pb (251.3 ppm; 34.4), Sb (176.3 ppm; 28.8), Ag (5.8 ppm; 0.7), and Mo (2.8 ppm; 2.1).

Contrary to py-0a, py-0b is prevalent in most deposits in the KCD area (Fig. 9, Table 2). The median values for this type of pyrite are comparatively lower than those for py-0a, exhibiting a consistent trend across deposits within overall median of Au (0.18 ppm; 6.4), As (230.9 ppm; 1640.3), Mo (0.004 ppm; 0.09), Pb (15.2 ppm; 23.2), Ag (0.4 ppm; 0.5), and Bi (3.4 ppm; 5.0). Py-0b displays a similar pattern of trace element content among deposits for Ag, Sb, Pb, Cu, Bi, Co, Ni, and Te when compared to py-1 and py-2. However, at the Agbarabo deposit, several outliers of trace elements were exclusively observed in one sample (YWK086). In this particular sample, trace elements are elevated, including Bi (25.3 ppm), Ni (1007.4 ppm), Sb (41.4 ppm), Mn (48.9 ppm), Co (1654.5 ppm), Au (41.2 ppm), and Te (7.6 ppm), with higher mean values compared to other deposits.

Py-1 (Fig. 9, Table 2) exhibits an inconsistent trace element pattern across all deposits. Although lower in comparison to py-0a, this pyrite type displays high median values in relation to other pyrites, varying based on the specific deposits. Notably, Au is low across all deposit 0.4 ppm (20.8) but present a relatively elevated concentration in Agbarabo, Tete Bakangwe, and Kalimva deposit, with median values of 3.41 ppm (10.2), 2.02 ppm (1.4), and 25.75 ppm (40.8), respectively. At Kalimva and Tete Bakangwe, py-1 demonstrates considerable median values for Mn, Zn, As, Mo, W, and Bi. Notably, at Tete Bakangwe, As (1638.7 ppm; 231.6), Mo (70.5 ppm; 37.5), and Bi (9.8 ppm; 0.2) exhibit the highest median values compared to Kalimva.

Py-2 (Fig. 9, Table 2) demonstrates significant median values with a wide range of variation for various trace elements across the district, particularly for Au, with an overall median of 3.1 ppm (32.8). Notably, KCD and Kalimva exhibit predominant median values of Au with 4.3 ppm (18.6) and 20.9 ppm (72.5), respectively, while Kombokolo and Tete Bakangwe show relatively lower values, displaying 0.18 ppm (0.2) and 0.48 ppm (0.8), respectively. The KCD deposit also stands out with notable values for Ag at 0.7 ppm (3), while Kombokolo exhibits a median Cu value of 8.6 ppm (17.1). Cobalt is generally present at concentrations below 100 ppm, with Agbarabo displaying a minimum value of 487.2 ppm (142) (2 spot analyses). However, As concentrations seem consistent in the same range across the district. The maximum value at KCD reaches 20894.3 ppm, and the median is 5569.4 ppm (5632.3).

Py-3 (Fig. 9, Table 2) represents a pyrite generation characterized by significant depletion in almost all trace elements, displaying median values one or two orders of magnitude lower than other pyrite types. The median Au concentrations (0.02 ppm; 0.1) of this pyrite class are comparable to those of py-4a and py-5. However, it exhibits higher Pb values (3.9 ppm; 7.3) than py-4a (0.81 ppm; 2.6), and the Co content is relatively similar to that of py-5. Notably, its distinctive feature lies in the extremely low proportions of As, ranging from 0.01 to 3.63 ppm (median 0.02 ppm; 0.5). The Bi values show considerable variability and higher proportions than those of py-5. Additionally, Py-3 displays elevated median values of W at 29.7 ppm (16.2) and Se at 18.2 ppm (25.0).

Py-4a (Fig. 9, Table 2) is depleted in trace elements, including Au (0.06 ppm; 0.1), As (634.5 ppm; 1626), Ag, Sb, Te, Pb, Bi, Cu, Mo, Cd, In, Sn, Cs, La, W, Hg, TI, Ga, Gd, Ge, and Zn. These trace element proportions are relatively similar in all deposits, with a wide range at KCD, Agbarabo, and Tete Bakangwe. However, it consistently demonstrates significant mean values of Co, Ni, and Se across all deposits. At Agbarabo, Au (0.32 ppm; 0.2 ppm) and Co (1078.86 ppm; 520.1) content have a relatively high average compared to the other deposits.

Py-4b (Fig. 9, Table 2) exhibits high median values for Au, As, Ag, Sb, Te, Pb, Bi, Cu, Ni, and Co. In KCD, the median values for these elements are Au (5.5 ppm; 6.6), As (4392.1 ppm; 3369.7), Ag (1.6 ppm; 1.67), Sb (23.6 ppm; 28.8), Te (2.0 ppm; 3.4), Pb (52.3 ppm; 344.1), Bi (4.3 ppm; 4.7), and Cu (43.4 ppm; 738.6). At Kalimva, As (10755.7 ppm; 7328.2) shows the highest mean value compared to the other pyrite types, while Te (21.3 ppm; 0.6) exhibits the highest mean value at Tete Bakangwe.

Py-5 (Fig. 9, Table 2) is depleted in several trace elements similar to py-4a with relatively analogous proportions over the district, presenting high median values of Co (492.3 ppm; 3433.5) and Se (24.1 ppm; 8.4) at Kalimva. Moreover, the median proportions of Ni are also relatively high in this generation of pyrite. Despite being a single sample (YWK070), ten spot analyses in py-5 from Pakaka show As values between 3323.4 and 5452.7 ppm. This is followed by Agbarabo values ranging from 799.3 to 6031.9 ppm. Arsenic also shows proportions equivalent to the py-4a. However, Pb values are highly depleted in most deposits, with most proportions below 0.1 ppm. However, values at Pakaka, although not very representative, are high, ranging from 0.06 to 12.6 ppm.

4.4. LA-ICP-MS trace element imaging

Due to the complementary nature of LA-ICP-MS elemental distribution mapping and spot analysis (e.g., Babedi et al., 2022), we conducted elemental mapping analyses on seven pyrite grains from the Kibali gold district (Appendix A.2) to add additional data to the spot analyses collected. The selection of pyrite grains was performed carefully based on their generation and mineral assemblage (Table 1), including four samples from KCD (Fig. 10a, b, c, d), and one sample each from Agbarabo (Fig. 10e), Tete Bakangwe (Fig. 10f), and Kalimva (Fig. 10g). The spatial patterns of trace elements distribution in py-2 samples from deformed conglomerates at KCD (Fig. 10a) and altered BIF at Tete Bakangwe (Fig. 10f) are similar.

The core (py-2) has relatively elevated levels of Au, As, Bi, Cr, Cu, Gd,

Table 2
Statistical summary of selected LA-ICP-MS trace element concentrations of pyrite generations from the Kibali Gold District. All values are expressed in ppm.

Deposit	Pyrite-type		Au	As	Ag	Sb	Ni	Co	Se	Te	Pb	Bi	Cu
	LOD		0.02	0.10	0.03	0.01	0.15	0.03	0.41	0.04	0.02	0.01	0.11
KCD	Py-0b	Mean	0.90	1068	0.80	35.78	83.09	143.3	8.92	1.30	38.90	5.18	39.92
	n = 20	Median	0.22	231.8	0.80	21.72	58.85	104.7	4.12	0.82	35.52	3.38	22.40
		Sd	2.02	2223	0.53	31.34	67.45	134.0	11.64	2.13	24.87	4.63	56.31
	Py-1	Mean	0.40	1336	0.67	20.85	125.5	75.29	2.81	0.32	48.78	1.10	55.90
	n = 29	Median	0.12	436.8	0.26	10.19	32.16	10.86	0.12	0.01	15.04	0.10	9.30
		Sd	1.15	2103	1.00	24.84	247.1	136.0	4.41	0.68	72.07	1.88	134.1
	Py-2	Mean	10.98	6352	2.01	16.54	67.93	53.76	11.99	1.71	55.92	1.92	165.9
	n = 50	Median	4.34	5569	0.68	10.68	25.83	24.36	11.10	0.80	25.30	1.18	16.82
		Sd	18.66	5632	3.01	16.24	91.15	66.68	9.82	2.16	88.18	2.38	375.2
	Py-3	Mean	0.07	0.40	0.02	5.91	57.55	31.09	24.56	0.28	6.40	0.13	2.75
	n = 16	Median	0.02	0.02	0.01	3.08	27.54	20.82	18.22	0.23	3.87	0.01	1.18
		Sd	0.13	0.93	0.02	6.18	67.42	36.19	25.00	0.32	7.31	0.38	5.35
	n = 15	Median	0.03	374.1	0.03	0.27	82.05	203.7	6.85	0.03	0.81	0.13	0.57
		Sd	0.83	1825	0.10	2.60	393.1	514.3	9.38	0.31	2.21	0.58	3.73
	Py-4b	Mean	7.08	4769	2.06	32.60	228.4	168.9	7.59	3.11	204.6	5.41	456.0
	n = 22	Median	5.49	4392	1.60	23.16	87.43	120.13	2.68	2.03	52.32	4.26	43.38
		Sd	6.62	3369	1.68	28.84	258.1	174.38	9.60	3.49	344.1	4.79	738.7
	Py-5	Mean	0.08	269.5	0.01	0.00	45.77	12.34	13.83	0.08	0.01	0.00	0.07
	n = 2	Median	0.08	269.5	0.01	0.00	45.77	12.34	13.83	0.08	0.01	0.00	0.07
		Sd	0.10	127.4	0.00	0.00	51.86	7.05	15.22	0.04	0.00	0.00	0.07
Gorumbwa	Py-4a	Mean	0.19	472.3	2.05	34.87	885.8	3551	13.45	0.73	2.93	1.26	178.34
	n = 2	Median	0.19	472.3	2.05	34.87	885.8	3551	13.45	0.73	2.93	1.26	178.34
		Sd	0.14	58.36	1.32	25.20	247.9	76.89	4.66	0.56	1.58	0.77	140.40
	Py-4b	Mean	0.21	570.8	6.80	187.92	929.3	3762	10.16	0.60	11.45	2.60	97.04
	n = 2	Median	0.21	570.8	6.80	187.92	929.3	3762	10.16	0.60	11.45	2.60	97.04
		Sd	0.17	475.3	4.76	157.26	128.9	2287	2.34	0.17	9.41	1.10	18.85
Kombokolo	Py-0b	Mean	0.21	558.8	0.21	5.26	33.97	136.9	13.40	1.14	10.33	5.75	10.30
	n = 13	Median	0.19	239.0	0.09	4.41	23.60	88.68	10.91	0.90	7.44	4.96	7.40
		Sd	0.15	708.1	0.23	3.85	23.16	134.92	12.49	1.06	8.50	3.39	8.41
	Py-2	Mean	0.23	1967.1	0.34	1.67	16.22	15.36	7.89	0.38	5.93	0.84	13.18
	n = 9	Median	0.18	1525	0.33	0.99	11.38	3.97	6.72	0.22	3.80	0.15	8.58
		Sd	0.15	1224	0.22	1.51	15.67	20.88	6.11	0.36	8.06	1.59	17.17
	Py-4a	Mean	0.08	646.3	0.07	0.32	56.07	67.97	19.77	0.32	1.76	0.54	2.06
	n = 5	Median	0.06	345.7	0.06	0.21	56.93	66.27	16.53	0.30	1.35	0.24	1.29
		Sd	0.05	711.7	0.06	0.19	36.94	46.85	9.99	0.31	1.79	0.53	1.19
	Py-4b	Mean	0.13	970.9	0.40	1.15	1.99	0.34	5.20	0.12	2.67	0.40	8.86
	n = 1	Median	0.13	970.9	0.40	1.15	1.99	0.34	5.20	0.12	2.67	0.40	8.86
		Sd	0.00	0.00	0.00	0.00	0.00	0.00	0.00	0.00	0.00	0.00	0.00
	Py-5	Mean	0.02	139.9	0.03	0.01	93.61	259.3	19.69	0.13	0.01	0.03	0.35
	n = 5	Median	0.02	35.72	0.01	0.00	58.94	173.3	21.34	0.15	0.01	0.01	0.13
		Sd	0.02	242.7	0.05	0.01	91.37	245.2	10.60	0.10	0.02	0.04	0.48
Agbarabo	Py-0b	Mean	41.26	1854	1.08	41.37	1007	1654	15.67	7.58	33.39	25.29	26.88
	n = 1	Median	41.26	1854	1.08	41.37	1007	1654	15.67	7.58	33.39	25.29	26.88
		Sd	0.00	0.00	0.00	0.00	0.00	0.00	0.00	0.00	0.00	0.00	0.00
	Py-1	Mean	10.07	2770	2.69	21.28	741.1	1097	13.80	3.95	37.41	8.98	268.1
	n = 2	Median	3.41	2472	0.91	11.82	714.6	900.1	11.54	2.85	35.06	5.89	44.52
		Sd	10.23	1159	4.44	17.60	333.9	687.0	6.03	2.91	26.81	6.08	568.5
	Py-2	Mean	6.92	1984	1.07	6.01	587.7	1234	13.91	4.63	14.57	5.04	141.5
	n = 2	Median	6.92	1984	1.07	6.01	587.7	1234	13.91	4.63	14.57	5.04	141.5
		Sd	8.48	719.6	0.01	2.76	142.0	1128	2.59	2.85	3.21	2.06	196.7
	Py-4a	Mean	0.32	1300	0.11	1.39	830.6	1078	12.90	0.66	1.38	1.39	0.63
	n = 5	Median	0.39	1278	0.06	0.54	858.6	1196	12.39	0.03	0.49	0.66	0.49
		Sd	0.28	690.6	0.13	1.48	297.6	520.1	2.96	0.91	2.07	1.60	0.53
	Py-5	Mean	0.30	2200	0.04	0.11	973.8	535.7	16.35	0.01	0.08	0.05	0.07
	n = 5	Median	0.01	1635	0.01	0.03	926.6	280.9	15.26	0.01	0.10	0.02	0.03
		Sd	0.59	2184	0.09	0.13	161.87	442.6	4.06	0.00	0.05	0.05	0.06
Pakaka	Py-1	Mean	0.30	1742	0.06	3.26	2627	284.4	30.43	0.08	34.16	0.02	16.79
	n = 1	Median	0.30	1742	0.06	3.26	2627	284.4	30.43	0.08	34.16	0.02	16.79
		Sd	0.00	0.00	0.00	0.00	0.00	0.00	0.00	0.00	0.00	0.00	0.00
	Py-5	Mean	0.02	8249	0.05	0.88	1477	6130	25.08	0.11	2.29	0.13	0.59
	n = 10	Median	0.00	7887	0.01	0.18	1493	5166	25.39	0.01	0.43	0.03	0.03
		Sd	0.03	3714	0.14	2.22	796.9	4071	2.64	0.28	4.04	0.28	1.10
Tete Bakangwe	Py-0b	Mean	0.31	478.4	0.22	4.91	144.8	144.1	10.85	0.90	7.50	2.67	2.24
	n = 7	Median	0.07	103.5	0.12	1.25	140.3	134.5	10.34	0.97	3.74	1.86	2.61
		Sd	0.67	960.3	0.21	5.60	87.57	98.45	3.43	0.65	8.83	2.47	1.76
	Py-1	Mean	2.03	1638	2.30	9.42	137.0	165.2	10.22	6.49	42.61	9.87	199.8
	n = 2	Median	2.03	1638	2.30	9.42	137.0	165.2	10.22	6.49	42.61	9.87	199.8
		Sd	1.48	231.6	1.49	2.86	4.25	113.8	0.05	3.06	18.14	0.27	255.5
	Py-2	Mean	0.75	877.3	2.32	4.45	88.04	113.6	10.01	5.96	16.95	5.80	244.90
	n = 8	Median	0.48	421.8	0.87	3.07	81.74	79.03	10.14	4.15	8.31	4.06	6.82
		Sd	0.85	934.5	2.56	4.11	63.24	97.05	4.64	7.95	19.08	6.67	564.18
	Py-4a	Mean	0.11	1079	0.06	0.24	142.5	113.6	10.78	0.64	0.72	0.37	0.62
	n = 11	Median	0.04	150.5	0.04	0.20	141.6	48.46	10.17	0.43	0.67	0.27	0.47

(continued on next page)

Table 2 (*continued*)

Deposit	Pyrite-type		Au	As	Ag	Sb	Ni	Co	Se	Te	Pb	Bi	Cu
		Sd	0.17	1753	0.07	0.19	127.6	207.2	7.12	0.53	0.53	0.28	0.54
	Py-4b	Mean	2.37	1234	1.77	6.21	73.90	38.08	6.41	21.34	37.96	7.09	428.67
	n = 2	Median	2.37	1234	1.77	6.21	73.90	38.08	6.41	21.34	37.96	7.09	428.67
		Sd	1.62	1006	0.45	2.59	16.72	25.71	4.15	6.99	14.25	6.24	470.1
	Py-5	Mean	0.00	1027	0.01	0.01	100.9	380.1	14.04	0.25	0.02	0.02	0.07
	n = 6	Median	0.00	751.9	0.01	0.01	77.01	77.06	14.31	0.20	0.00	0.01	0.03
		Sd	0.00	1155	0.00	0.01	107.7	753.1	3.64	0.28	0.02	0.03	0.06
Kalimva	Py-0a	Mean	15.18	9210	5.83	184.6	246.3	340.6	4.08	2.32	259.1	58.14	44.35
	n = 7	Median	15.62	8895	5.78	176.3	248.4	337.8	4.18	2.32	251.3	54.66	43.36
		Sd	1.63	717.8	0.73	28.89	27.89	41.70	0.77	0.41	34.46	10.30	3.66
	Py-1	Mean	34.64	11725	7.14	37.49	191.7	196.7	5.45	0.69	87.49	12.00	31.28
	n = 8	Median	25.75	11975	3.18	29.73	158.1	145.5	5.11	0.61	78.25	10.57	23.76
		Sd	40.82	5308	11.96	25.82	102.7	139.0	2.30	0.34	44.64	7.61	20.01
	Py-2	Mean	39.30	11978	2.51	9.57	70.47	98.92	5.94	0.57	39.12	10.75	27.41
	n = 12	Median	20.99	10929	1.42	7.75	49.44	69.47	5.34	0.40	36.78	9.64	13.78
		Sd	72.49	7328	3.19	8.39	67.07	87.57	3.58	0.67	30.54	10.17	45.39
	Py-3	Mean	0.02	0.02	0.04	4.45	1702	124.7	9.64	0.05	9.83	0.18	0.25
	n = 1	Median	0.02	0.02	0.04	4.45	1702	124.7	9.64	0.05	9.83	0.18	0.25
		Sd	0.00	0.00	0.00	0.00	0.00	0.00	0.00	0.00	0.00	0.00	0.00
	Py-4a	Mean	0.09	1566	0.08	0.37	68.29	749.9	12.03	0.88	2.72	1.28	0.69
	n = 9	Median	0.06	850.6	0.03	0.11	44.58	49.32	4.86	0.10	0.84	0.22	0.19
		Sd	0.12	2131	0.12	0.62	63.80	2039	14.64	1.55	4.82	2.81	1.46
	Py-4b	Mean	23.37	12069	3.11	15.40	80.90	115.1	4.56	0.42	254.7	12.68	12.76
	n = 8	Median	21.68	10755	1.30	7.74	58.99	73.34	4.50	0.17	39.51	10.78	11.86
		Sd	22.38	4836	4.99	16.17	72.29	114.9	2.74	0.48	554.3	11.48	8.76
	Py-5	Mean	0.00	2423	0.01	0.01	248.9	810.6	22.95	0.11	0.01	0.01	0.05
	n = 6	Median	0.00	2458	0.01	0.00	250.1	394.5	24.10	0.08	0.00	0.00	0.02
		Sd	0.00	992.0	0.00	0.01	130.3	1261	12.55	0.11	0.01	0.02	0.06

LOD: Low detection limit; Sd: Standard deviation.

La, Mn, Pb, Sb, Ti, V, W, and Zn compared to the rim (py-4a). The gold concentration tends to be more enriched in the core of py-2 and decreases towards contact with py-4a. In contrast, As tends to increase towards the contact with py-4a. The other elements are almost homogeneously distributed in py-2. However, the py-4a is relatively enriched in Co, Ni, Se, and Te in the outer zone with a sporadic elevated concentration of Cs, Cr, Bi, Sb, V, and W.

Fig. 10b highlights the trace elements in py-1 within a barren texture-destructive quartz-carbonate altered BIF protolith. The trace elements exhibit homogeneously low concentrations, except for Co, Ni, Mn, Cu, Cr, Zn, and As, which are concentrated in the outer zone of the pyrite grain. Antimony (Sb) occurs in the core, with a higher concentration in one part of the outermost area of the core.

Furthermore, the LA-ICP-MS map of py-4b grains (Fig. 10c and d) from the chlorite-altered conglomerate sample (YWK091), collected in the proximity of a mafic dyke intrusion that altered the pyrite grains with ~10 μm chlorite mineral occurrences (Fig. 8c and d), reveals an oscillatory zonation of As, Co, Bi, Ni, Pb, and Sb from the core to the outer zone. Gold and Cu are elevated in the outer core, while Mo is exclusively concentrated in the inner core (Appendix A.2).

The LA-ICP-MS trace element map from the Agbarabo deposit on py-4a (Fig. 10e) shows low concentrations of most elements in the pyrite grain, including Au, Ag, Ga, Cs, Cu, Mn, and Zn. Bismuth, Te, and Sb exhibit an irregular network pattern in the pyrite grain, while the outermost zone is enriched in V, Cr, Ga, Cs, and Zn. Nickel and Co present homogeneous concentrations.

In the Kalimva deposit, the LA-ICP-MS multi-element imaging data performed on one grain of py-0a (Fig. 10g) reveal that most elements (Ag, Au, As, Sb, Co, Pb, Cu, Bi, and W) have relatively similar spatial distribution and mainly occur in the central part of the py-0a grain with some elevated spots. However, Mn, Mo, Gd, La, and Zn are relatively depleted in the central region and enriched at the edge of the pyrite grain.

4.5. *Sulfur isotope analyses of pyrite*

The results obtained from in-situ S isotopic compositions from the Kibali gold district are presented in Fig. 11, and Appendix A.3. The $\delta^{34}S$ values of pyrite obtained from 60 spots analysis ranged from −0.05 to 7.6 ‰ (Fig. 11), with a mean of 3.3 ‰ (standard deviation is 1.8). The py-0a (n = 6) exhibits a slight variation (Fig. 11a and b), with values ranking near-zero from 0.5 to 1.8 ‰, whereas the py-1 (n = 7) displays values (Fig. 11a and b) ranging between 2.2 and 2.7 ‰ (mean 2.4 ‰). However, the py-2 (n = 20) has a wide range compared to other pyrite types (Fig. 11a and b), from −0.05 to 5.4 ‰ (mean of 2.7 ‰) followed by py-4a (n = 14) (Fig. 11a, b, c) which are between 1.6 and 5.7 ‰ (mean 3.7 ‰). The lowest $\delta^{34}S$ values of the py-2 are recorded from heavily deformed conglomerate sample YWK007 (Fig. 11a and b) containing subrounded pyrite forms. In addition, the py-2 from barren quartz-carbonate altered sample YWK012 (0.09 g/t Au) records low values of $\delta^{34}S$ compared to the mineralized quartz-carbonate altered rock (YWK025 = 16.1 g/t Au) and BIF (YWK009 = 11.5 g/t Au and YWK061 = 6.28 g/t Au, Fig. 11c) samples (Fig. 11). The py-3 (n = 7) is ranked between 3.1 and 4.6 ‰ (4.1 ‰ mean), while the py-4b (n = 6) has the highest $\delta^{34}S$ values from 5.36 to 7.6 ‰ with a mean of 6.4 ‰.

5. Discussion

Using a novel uniform manifold approximation and projection (UMAP) technique to refine our assignment of pyrite to several generations of genesis (Mpaka and von der Heyden, 2024 this issue), we have identified eight discrete classes of pyrite that exist in the Kibali gold district (Fig. 1). A drawback of our study is the somewhat limited number of samples for which we have detailed LA-ICP-MS mineral chemistry data (19 samples). However, using knowledge of the respective ore bodies evaluated and by careful examination of the petrographic textures of a much larger sample set (91 samples), we extrapolate our interpretations of the different pyrite classes to provide insights into the genesis of gold mineralization on the district scale.

5.1. *Pyrite chemical evolution and significance*

The Kibali gold district experienced a complex basin evolution, deformation, magmatism, metamorphism and hydrothermal activity

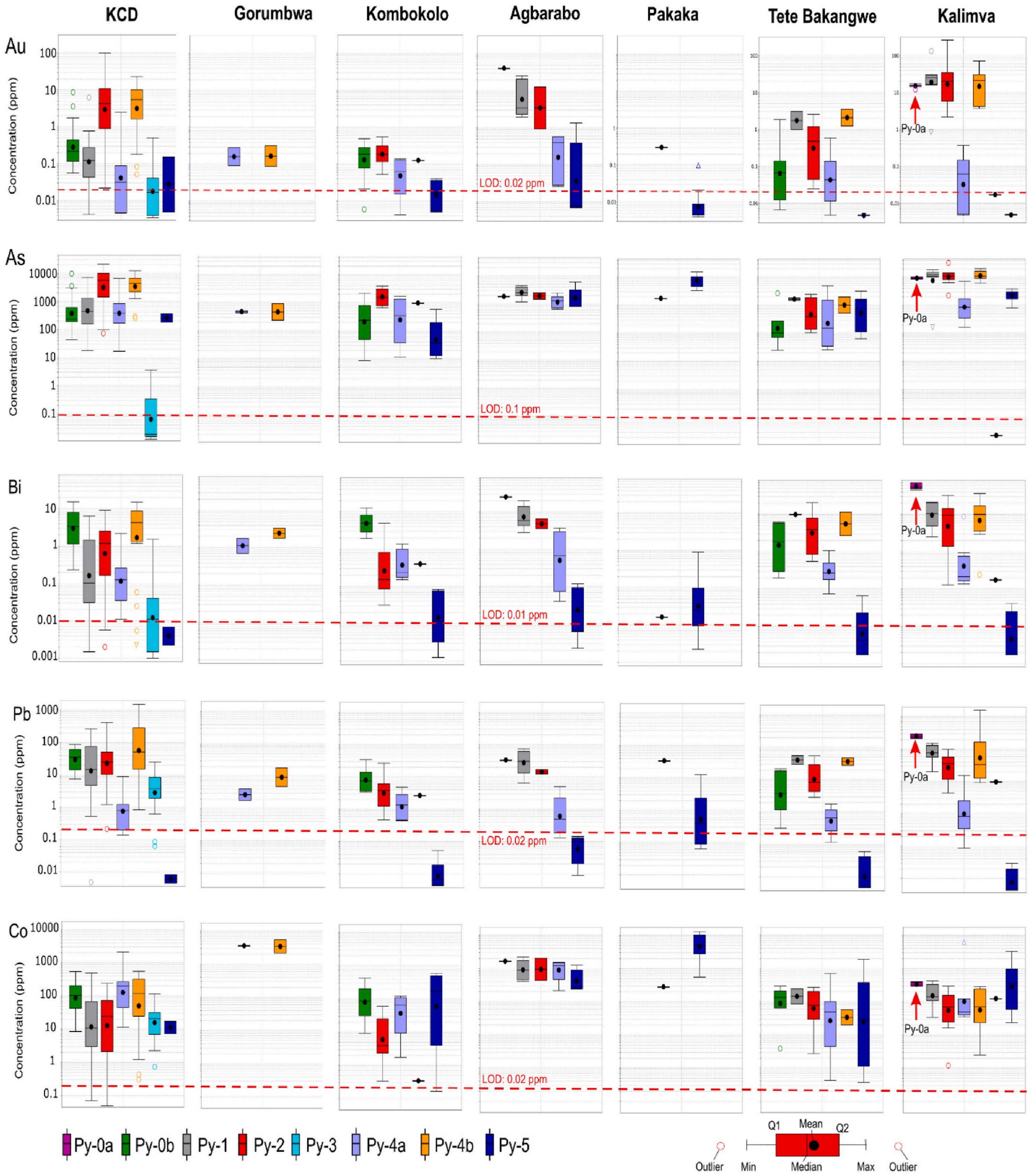

Fig. 9. Box-and-whisker plot of selected trace-element concentrations of pyrite types from each deposit in the Kibali district. Boxes show data between the 25th (Q1) and 75th (Q2) percentiles, and the upper and lower limits extend 1.5 times beyond the interquartile range towards the maximum (Max) and minimum (Min) values, respectively. All values falling outside of the mentioned range are identified as an outlier and plotted outside of the box. Abbreviation: LOD: limit of detection.

(Bird, 2016; Allibone et al., 2020; Mpaka et al., 2023). The older basin rocks in the Kalimva deposit preserve the only identified occurrence of py-0a class, characterized by small-sized (<20 μm across) framboidal sooty grains. The consistently elevated trace element composition (As, Au, Sb, Pb, Hg, Ni, Cu, Bi, Cd, Mo, and Sn) and near-zero $\delta^{34}S$ values (mean 1.3 ‰) suggest rapid pyrite formation from supersaturated pore waters rich in Fe and H_2S, likely sourced from seawater sulfate and volcanic S (Steadman et al., 2015; Gregory et al., 2019). Furthermore,

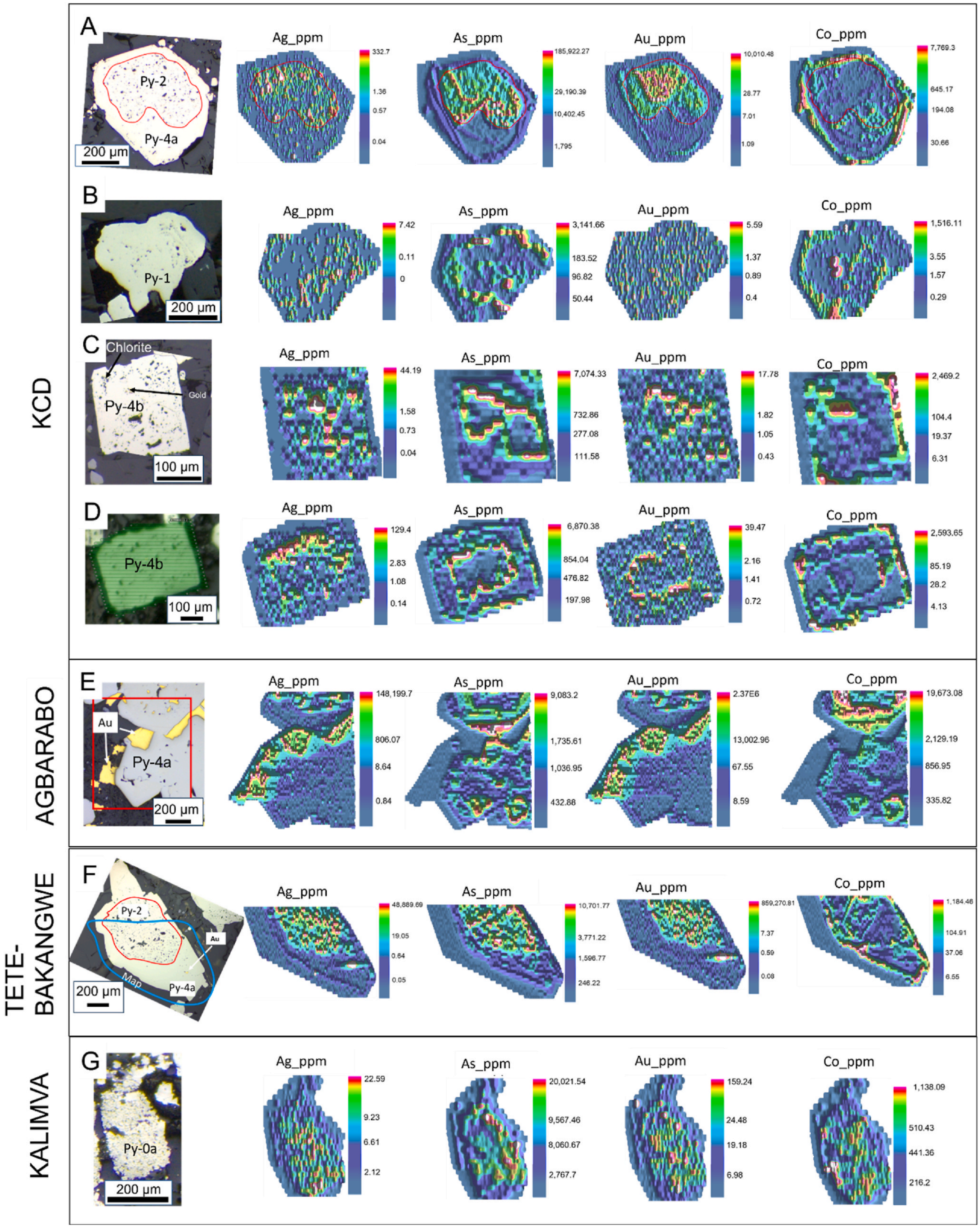

Fig. 10. LA–ICP–MS map of selected trace element of pyrite grains. **A.** Map of py-2 and py-4a in the clastic sediment from the KCD deposit (5000 lodes, YWK007 with whole-rock Au = 48.3 g/t). **B.** Map of py-1 in the destructive quartz - Fe carbonate altered BIF (ACSA) from the KCD deposit (12000 lodes, YWK012 with whole-rock Au = 0.09 g/t). **C** and **D.** Map of py-4b in the clastic sediment from the KCD deposit (9000 lodes, YWK091 with whole-rock Au = 33.3 g/t). **E.** Map of py-4a in the clastic sediment from the Agbarabo deposit (YWK086 with whole-rock Au = 129 g/t). **F.** Map of py-2 and py-4a in the BIF from the Tete Bakangwe deposit (YWK061 with whole-rock Au = 6.28 g/t). **G.** Map of py-0a in the volcaniclastic sediment from the Kalimva deposit (YWK041 with whole-rock Au = 20.2 g/t).

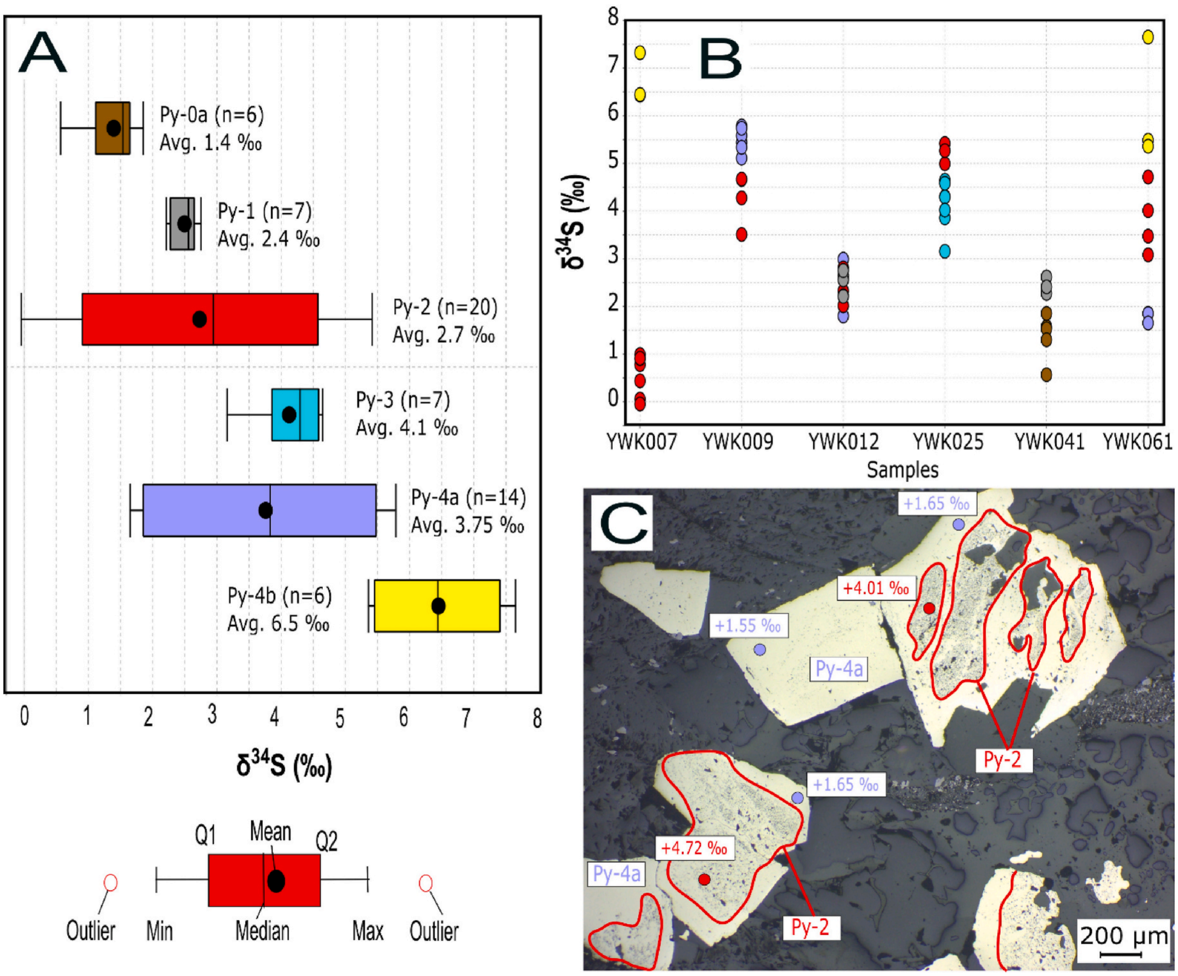

Fig. 11. Different SIMS results representing the $\delta^{34}S$ (‰) values of pyrite in the Kibali gold district. **A.** Box-and-whisker plot of $\delta^{34}S$ (‰) values of pyrite types. The data representation involves delineating information within the interquartile range, specifically between the 25th (Q1) and 75th (Q3) percentiles. The upper and lower limits are extended by 1.5 times the interquartile range towards the maximum (Max) and minimum (Min) values, respectively. Any data points surpassing this specified range are recognized as outliers and displayed outside the designated box. B. $\delta^{34}S$ variation from pyrite types with YWK007, YWK009, YWK012 and YWK025 from KCD deposit, YWK041 from Kalimva deposit and YWK061 from Tete Bakangwe deposit. **C.** Reflected light photomicrographs from YWK061 sample with spots of SIMS analysis.

the elevated concentration of Mo (median 2.8 ppm), V and Cr suggests a probable local oxidation during the formation of this pyrite before the Great Oxidation Event (GOE1) (e.g., Large et al., 2014; Steadman et al., 2015, 2020; Du et al., 2021; Wang et al., 2021).

The near-zero $\delta^{34}S$ values of the py-0a are indicative of potential bacterial reduction of seawater sulfate (e.g., Chang et al., 2008; Fike et al., 2015; Zhao et al., 2018). These findings align with the positive light S isotope values found in sedimentary nodule pyrite, such as those documented in the Golden Mile Deposit in the Kalgoorlie terrane (Steadman et al., 2015). Previous research (Fischer et al., 2014; Fike et al., 2015; Li et al., 2017; Bosco-Santos et al., 2022) on sedimentary pyrite from the Archean period (>2.5 Ga) has indicated relatively minor $\delta^{34}S$ variations (~0‰), with average values resembling those of the bulk silicate earth. Their suggests potential scenarios, ranging from limited biological cycling to restricted induced fractionation during dissimilatory sulfate reduction (Wacey et al., 2010; Fischer et al., 2014; Fike et al., 2015; Li et al., 2017; Meyer et al., 2017; Bosco-Santos et al., 2022).

However, challenges arise from the scarcity of sulfate minerals in Archean sedimentary records, given that sedimentary pyrite acts as the primary geochemical sink for sulfur in Archean oceans (Fischer et al., 2014; Fike et al., 2015; Meyer et al., 2017). This one-sink Archean sulfur cycle remains not fully understood, requiring a comprehensive understanding of how sedimentary successions preserve isotopic signatures through complex sulfur mineralization histories (Fike et al., 2015; Bosco-Santos et al., 2022). Despite these challenges, it is possible that py-0a in our study represents remnants of syn-diagenetic pyrite from the old basin in the Kibali gold district (>2.64 Ga). Notably, due to their elevated Au content (median 15.6 ppm), these pyrites may serve as a substantial repository of gold for potential mobilization and re-concentration during later deformation and metamorphism in the Kibali gold district.

The lowermost thrust stack in the Kibali district is represented by rock types of the 'later basin', mainly comprised of clastic and chemical sedimentary rocks such as BIF, chert, conglomerate to siltstone, carbonaceous shale, and a lesser amount of volcanic and volcaniclastic rock-types (Allibone et al., 2020; Mpaka et al., 2023). The earliest formed pyrite in this sequence is py-0b, which is typically fine-grained (<40 µm), found along the foliation fabric, and disseminated within the silicate matrix. The py-0b generation is interpreted as a late diagenetic to early metamorphic origin occurring during the later basin's formation or orogeny (e.g., Large et al., 2014; Majumdar et al., 2019). The py-0b exhibits a different trace element signature compared to py-0a, featuring non-specific elevated trace elements, including Au, As, Sb, Pb, and among others, when compared to py-0a and other pyrite-types (Fig. 9). Their small size and euhedral shape support low-temperature precipitation, as discussed by previous scholars (e.g., Large et al., 2007; Chang et al., 2022). However, the low concentration of trace elements compared to the py-0a and other hydrothermal pyrite excludes this type as a primary source of gold and trace elements. These lines of evidence suggest different precipitation environments for the two early pyrite types (py-0a, and py-0b), although higher-density sampling may reveal more extensive distributions of each within the two basins.

However, the pyrite py-1 generation has relatively low levels of Au (0.4 ppm; 20.8) and elevated median with large standard deviations such as Ti (88.1 ppm; 2088.0), Ag (0.5 ppm; 5.6), Cr (2.2 ppm; 26.2), and V (1.7 ppm; 19.3), which can be linked to nano- and micro-inclusions (e.g., Winderbaum et al., 2012; Mathieu, 2019). Petrographic observations reveal that this generation represents the metamorphic growth stages of recrystallization of both py-0a and py-0b (Figs. 6 and 7d and e), formed by solid-state aggregation of grains during ductile deformation (Gregory et al., 2015; Belousov et al., 2016; Tan et al., 2022). Py-1 (Fig. 8a and b) exhibits a plastically elongated form aligned with boudinaged and sheared quartz, indicating its formation before the cessation of ductile deformation (e.g., Chowdhury et al., 2020; Perret et al., 2022).

The pyrite generation py-2 is characterized by a porous texture dominated by elevated proportions of mineral inclusions (Fig. 6) and is widely distributed in the quartz-carbonate altered rocks. Py-2 exhibits high levels of trace elements, as shown in the spot trace element analyses (Fig. 9) and elemental maps (Fig. 10). This includes a high median Au concentration of up to 20.9 ppm (72.5) at Kalimva. The strong correlation between Au and As ($R^2 = 0.89$), also depicted in the elemental maps (Fig. 10), supports either a solid solution state of Au and As in this pyrite generation (Fig. 12a) or homogeneously-distributed nanoinclusions of arsenopyrite and/or native gold (Fleet and Mumin, 1997; Maddox et al., 1998; Simon et al., 1999; Reich et al., 2005; Zhu et al., 2011; Deditius et al., 2008, 2011; Velásquez et al., 2014; Pokrovski et al., 2019, 2021; Filimonova et al., 2020). The Au–As plot proposed by Reich et al. (2005) is generally interpreted such that data points below the line are considered as Au occurring in solid solution, while those above are considered as occurring as inclusions. In our dataset, as illustrated in Fig. 12a, data points predominantly fall within the solid solution zone, showing a relatively high correlation with high Au and As content in pyrite. However, in other pyrite samples without As-rich, a strong correlation is observed between Au and Ag and other elements like Te, Bi, Se, and Cu. This suggests the presence of nano- or micro-inclusions (tellurides, bismuthides, electrum, etc.) (e.g., Augustin and Gaboury, 2019), which is evident as this class of pyrite contains several inclusions and pores (Fig. 6).

The py-2 generation exhibits a wide range of $\delta^{34}S$ values, ranging from −0.05 to 5.4 ‰ (mean of 2.7 ‰), when considering all dataset compared to other pyrites (Fig. 11a and b). However, when examining individual samples, significant variations are not apparent (Fig. 11b). This suggests that the observed variability may be attributed to fluid-wall rock reactions during sulfidation and carbonation (Palin and Xu, 2000; Adomako-Ansah et al., 2013). Thus, the $\delta^{34}S$ values taken

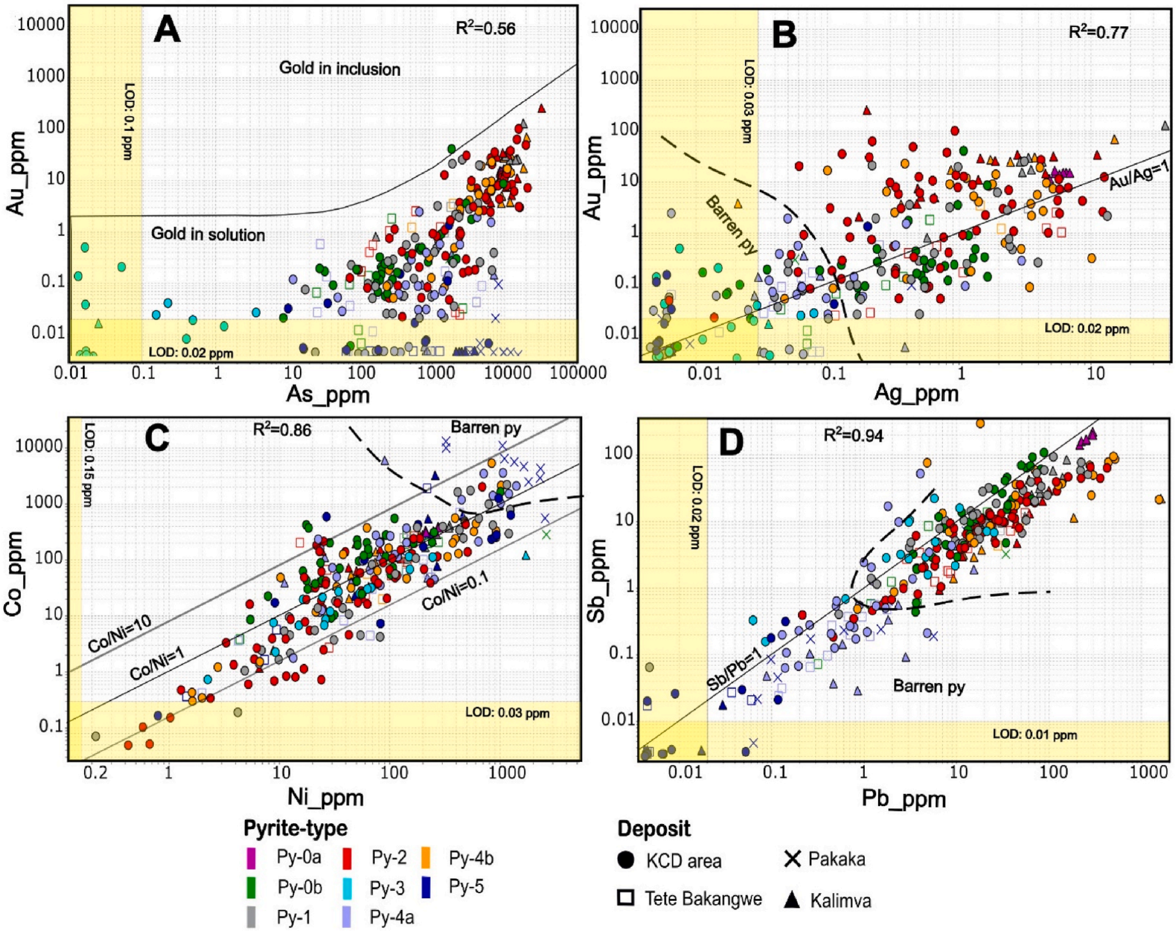

Fig. 12. The log biplot illustrates selected trace element spot analyses on pyrite types from the Kibali gold district. **A.** The Au–As plot illustrates the gold solubility fields proposed by Reich et al. (2005), with most points falling within the gold in solution field. Py-0a, py-1, py-2, and py-4b are dominant data points in the elevated Au, exceeding 1 ppm. **B.** The Au–Ag plot emphasizes a relatively strong correlation ($R^2 = 0.77$) within the pyrite trace element datasets, with Au barren pyrite exhibiting a depletion of Ag. **C.** The Co–Ni plot highlights the dominant pyrite trace element results within the area between Co/Ni = 10 and Co/Ni = 0.1. Most of the Au barren pyrite (py-4a and py-5) falls in the elevated Co and Ni region. **D.** The Sb–Pb plot reveals an elevated correlation ($R^2 = 0.94$) within the pyrite trace element dataset, indicating low values of Pb and Sb for Au barren pyrites (py-3, py-4a, and py-5). Abbreviations: LOD: limit of detection; R^2: correlation coefficient.

individually show that each lithology reacts differently from the other. Additionally, the presence of anhedral barite inclusions occurring next to the gold, and chalcopyrite grains within py-2 (Fig. 7b and c) in two samples suggests that ore fluid oxidation may play a role in the Au precipitation in this pyrite type (Phillips et al., 1986; Mccuaig and Kerrich, 1998; Hodkiewicz et al., 2009; Phillips, 2022). Based on the strong associations with Au, albeit by different mechanisms, this pyrite phase is identified as the first ore stage, associated with hydrothermal fluid flow and local sulfidation of Fe-rich lithotypes.

In contrast to py-2, py-3 is remarkably depleted in several trace elements, e.g., Au (0.02 ppm; 0.1), As (0.02 ppm; 0.5), and others, except for the highest Se (18.2 ppm; 25.0) and W (29.7 ppm; 16.2) compared to other pyrites (Fig. 9). This generation is characterized by the replacement of pyrrhotite in association with marcasite. An experimental study conducted by Qian et al. (2011) demonstrates that the replacement of pyrrhotite by pyrite results from a dissolution-reprecipitation process, whereas marcasite suggests S-poor hydrothermal fluids. In dissolution-reprecipitation reactions, the parent mineral dissolves in a fluid phase, promptly followed by the precipitation of the daughter mineral. This transformation can occur through Fe-loss or during the sulfidation reaction mechanism in the presence of aqueous H_2S or via an external oxidant (O_2) (Qian et al., 2011). The py-3 is replaced by siderite alteration, suggesting that this pyrite generation predates quartz-Fe-carbonate alteration associated with the ore stage ($FeS_2 + H_2O + H_2 + CO_2 \leftrightarrow FeCO_3 + 2\ H_2S$ (Kusebauch et al., 2018)). The depletion in trace element tenors may be related to 1) the low capacity for precursor pyrrhotite to incorporate trace elements into its crystal structure (Walker et al., 2020; Maurer et al., 2021; Lipko et al., 2022), 2) the involvement of a fluid depleted in its trace element, or perhaps most likely, 3) both considerations. Similarly, their $\delta^{34}S$ composition ranges from 3.1 to 4.6 ‰ (mean 4.1 ‰) and could reflect the S signature of either the precursor pyrrhotite or the py-3 fluid. The relatively limited data on this generation and its complex mineral association do not allow for unequivocal conclusions compared to other pyrite types, and further work will be needed.

The main ore-stage event is represented by the py-4a and py-4b generations, which both occur as rims on pre-existing pyrite nuclei (Fig. 6). The py-4a manifests as an unzoned rim, typically occurring on py-2 nuclei (Fig. 6c), and displays depleted levels of trace elements such as Au (median of 0.03 ppm (0.8) at KCD). The texture of py-4a has resulted from the removal of trace elements during metamorphic growth or recrystallization under moderate to non-boiling conditions, as supported by the homogeneous texture and occasional mineral inclusions (Kampmann et al., 2018; Román et al., 2019; Conn et al., 2019). In contrast, the pyrite rim py-4b (Fig. 6d) exhibits oscillatory As-zoning and develops generally on nuclei of py-2. It is characterized by elevated trace element concentrations, including Au and As, which, for example, at KCD, reach concentrations of 5.5 ppm (6.6) and 4392.1 ppm (3369.8), respectively (Fig. 9). This type of As-rich band zoning is observed in many gold deposits (e.g., Chouinard et al., 2005; Velásquez et al., 2014), where it is attributed to crystallographic incorporation of trace elements controlled by growth rate or the chemical evolution of the hydrothermal fluid (Barker et al., 2009; Barker and Cox, 2011; Peterson and Mavrogenes, 2014; Fougerouse et al., 2016). A positive correlation between Au and As ($r^2 = 0.86$) suggests preferential precipitation of Au in the As-rich layers. Arsenic-rich pyrites are commonly suggested to play a role in scavenging Au, but the exact mechanism remains controversial (Fleet and Mumin, 1997; Maddox et al., 1998; Simon et al., 1999; Zhu et al., 2011; Velásquez et al., 2014; Pokrovski et al., 2019, 2021). Proposed mechanisms include the nonstoichiometric substitution of S_2^{2-} by AsS^{3-}, surface electrochemical reaction, chemisorption, and local dissolution of arsenopyrite during fluid-rock interaction (Fleet and Mumin, 1997; Maddox et al., 1998; Simon et al., 1999; Pokrovski et al., 2002, 2021; Velásquez et al., 2014).

The logarithm biplot in Fig. 12 provides a distinct separation (dot line) between barren pyrites (Au < 0.5 ppm), encompassing py-3, py-4a, and py-5, and auriferous classes like py-0, py-2, and py-4b (Fig. 12). Barren pyrites show low concentrations of trace elements such as Au, As, Sb, and Pb (Fig. 12a, b, d), coupled with heightened levels of Co and Ni (Fig. 12c). Conversely, mineralized pyrite (Au > 0.5 ppm), represented by gradationally py-0b and py-1 near the barren boundary, and followed by more elevated in Au–As, including py-2, py-0a, and py-4b, generally exhibits elevated values across most elements. The correlation between Pb–Sb, approximately 1:1, suggests the presence of nano-to micro-particles within the pyrite, including mineral inclusions like galena or boulangerite ($Pb_5Sb_4S_{11}$) (George et al., 2018; Babedi et al., 2022). The Co and Ni are primarily associated with py-5 and secondarily with py-4a, exhibiting flat and smooth depth profiles (Appendix A.4), indicative of their occurrence as solid solutions (e.g., Chowdhury et al., 2020; Keith et al., 2018). However, spikes in elemental maps of other pyrites (Fig. 10) indicate the presence of Co–Ni–Se-bearing mineral nanoparticles, as also observed in SEM analysis of our samples (Raič et al., 2022 and references therein).

Lastly, the cubic and euhedral py-5 pyrite generation exhibit typical characteristics of hydrothermal pyrite, as described by Large et al. (2007) and other researchers. The higher median concentrations of Co (492.3 ppm; 3433.5) (Fig. 12c), primarily observed within the mafic rock types, suggest a lithological influence. This pyrite generation formed during the late stages of metamorphism and represents the end-member phase of pyrite recrystallization in the Kibali district (e.g., Augustin and Gaboury, 2019). The py-5 contains lower concentrations of trace elements and Au (median 0.001 ppm; 0.01), indicating a low concentration of these elements in the hydrothermal fluid or due to inefficient Au deposition mechanism from an Au-rich fluid (Fig. 12). Additionally, the occurrence of large py-5 grains within the mafic igneous rocks, particularly in proximity to the mafic igneous margins, supports the input of local magmatic heat source components within the Kibali gold district. Furthermore, the euhedral pyrite associated with calcite minerals, commonly observed within the dolerite igneous rocks, suggests late-stage fluid circulation along the contact between the margin of igneous rocks and surrounding country rocks (Kattenhorn, 1994).

5.2. *Evolution of pyrite during deformation and remobilization*

The understanding of pyrite deformation has undergone significant advancements through various studies (Atkinson, 1976; McClay and Ellis, 1983; Marshall and Gilligan, 1987, 1993; Barrie et al., 2010; Perret et al., 2020, 2022; Zhao et al., 2021). Early work identified brittle deformation of pyrite across different geological contexts (Atkinson, 1976). Subsequent research demonstrated the occurrence of plastic deformation in pyrite at high temperatures, reaching up to 425 °C (Cox et al., 1981; McClay and Ellis, 1983). In the last decade, Barrie et al. (2009) suggested that the temperature threshold for plastic deformation in pyrite could be as low as ~200–260 °C. These processes can occur through solid-state ductile flow or through fluid-mediated or intragrain diffusion (Tomkins, 2007). Ductile deformation and metamorphism can significantly alter the distribution of mineral trace elements through remobilization during recrystallization, which can upgrade existing mineralization in ore shoots (e.g., Marshall and Gilligan, 1987, 1993; Marshall et al., 1998; Hastie et al., 2020). Additionally, it is well established that the deformation of pyrite after their formation promotes the expulsion of invisible gold (solid solution or nanoparticles) to form visible gold precipitates close to sulfides via coupled dissolution-reprecipitation (CDR) reactions (e.g., Large et al., 2009; Cook et al., 2013; Hastie et al., 2020).

Multiple pyrite generations exhibiting ductile deformation features (py-0 to py-4) in this study (Fig. 8) suggest prolonged sulfide precipitation and deformation, with some overlap. The presence of py-0a replaced by pyrrhotite through the reaction $2FeS_2 = 2FeS + S_2$ (Tomkins, 2007) during prograde metamorphism suggests a release of S during deformation. As depicted in Fig. 8a and b, pyrrhotite is observed in the wedge of deformation, and recrystallized py-1 is abundant in the dilatational site, indicating induced fluid-assisted recrystallization (Zhabin and Kremenetskiy, 1993; Marshall et al., 1998; Tomkins, 2007). These ductile deformation processes either in prograde or retrograde metamorphism, contributed to the remobilization of ore minerals (Tomkins, 2007), elucidating the transition from invisible gold concentration within pyrite to visible gold grains adjacent to pyrite. Observations of texture-destructive quartz-carbonate altered rocks indicate that ~87% of gold in the Kibali gold district is either included within, attached to, or remobilized and associated with sulfide minerals (Mpaka et al., 2023).

The remobilization process locally upgrades ore due to the relatively low solubility of gold in hydrothermal fluids (Hastie et al., 2020). This phenomenon is evident in various deposits globally, including the Yuhengtang Au Deposit in South China (Li et al., 2021), the gold deposits in the Archean Swayze Greenstone Belt in Canada (Hastie et al., 2020), and the Dabaiyang Te–Au deposit in China (Zhang et al., 2022). Li and coworkers (2021) suggest that the lower concentrations in the Yuhengtang Au Deposit of invisible gold in veinlet sulfides, compared to disseminated equivalents, are attributed to efficient scavenging. This scavenging process forms visible gold through infiltration-induced dissolution-reprecipitation reactions within the micropores of sulfides, facilitating the remobilization of invisible gold released from the sulfide lattice. In addition, this remobilization induces the coarsening of gold grains with a high-grade shoot, as suggested by previous research (e.g., Hastie et al., 2020; Voisey et al., 2020).

This could explain the observed high-grade shoot (>5 g/t Au) plunging NE in the Kibali gold district (Allibone et al., 2020; Mpaka et al., 2023), possibly resulting from deformation during the S_{n+1} event affecting the earliest formed mineralization (py-2 and py-4). Subsequently, S_{n+1} remobilizes through shearing, boudinaging, and folding ore minerals in tight folds (Fig. 8c and d), concentrating the high-grade shoot (e.g., Fougerouse et al., 2016; Hastie et al., 2020; Li et al., 2021; Ma et al., 2022; Zhang et al., 2022; Li et al., 2023). Furthermore, episodes of brittle deformation post-main ore stage are associated with fracturing of pre-existing pyrite (Fig. 8f). The py-5 generation, linked to brittle deformation and fluid flow, while barren itself, provided local sites for accumulating late remobilized gold in fractures (Fig. 8f). Reactivation events created permeability, facilitating fluid flow and resulting in the dissolution of chalcophile elements and invisible gold, reprecipitating as inclusions and larger interstitial grains within fractures (Fig. 8f) (Chowdhury et al., 2020; Cox, 1987; Vaughan and Kyin, 2004; Velásquez et al., 2014).

5.3. Source and evolution of S

Past studies have extensively investigated the role of S ligands in transporting gold in hydrothermal fluids (Ohmoto, 1972; Seal, 2006; Barker et al., 2009; Lawrence et al., 2013; Goldfarb and Groves, 2015). Changes in S isotope ratios have provided valuable insights into variations in the redox conditions of fluids that contribute to ore formation (Fleming and Bekken, 1995; Mccuaig and Kerrich, 1998). The bisulfide cation $Au(HS)^{2-}$ has been identified as the most important complexing cation for gold transport in hydrothermal environments (Hayashi and Ohmoto, 1991; Benning and Seward, 1996; Stefánsson and Seward, 2004; Williams-Jones et al., 2009; Meng et al., 2020). Thus, S isotope ratios in co-precipitated sulfides with gold have been used as a reliable tool for constraining the source of gold (Bierlein et al., 2004; Hodkiewicz et al., 2009; Rajabpour et al., 2017; Meng et al., 2020; Brueckner et al., 2021; Su et al., 2023). However, interpreting $\delta^{34}S$ isotopic data from mineral deposits remains challenging due to temperature and redox-dependent fractionation effects (Ohmoto and Goldhaber, 1997; Bierlein et al., 2004; Hodkiewicz et al., 2009), as well as the influences of fluid-wall rock reactions, phase separation, and mixing of magmatic-hydrothermal fluids (Phillips et al., 1986; Mccuaig and Kerrich, 1998; Hodkiewicz et al., 2009; Sun et al., 2020).

In the Kibali gold district, our investigation revealed a minimal variation in $\delta^{34}S$ values, ranging from −0.05 to 7.6 ‰ ($n = 60$) across all pyrite types with a mean of 3.3 ‰ (Fig. 11; Appendix A.3), consistent with earlier findings in the district, which ranged from −1.4 ‰ (the only negative value) to 7.5 ‰ ($n = 95$) (Bird, 2016). This suggests that $\delta^{34}S$ values either reflect a single origin (e.g., Bird, 2016) or a homogenization of S isotopes during metamorphism (e.g., Chang et al., 2008). It has been proposed that the primary source of S for deposits in the Kibali gold district could be the Kibalian sedimentary rock types and basalts during metamorphic devolatilization (Bird, 2016). However, it is essential to note that the observed $\delta^{34}S$ values in the district can overlap with various potential S reservoirs in Archean orogenic gold deposits. These potential sources encompass sulfur contributions from supracrustal rocks, such as volcano-sedimentary rocks prevalent in the ancient basin, mid to lower-crustal magmatic hydrothermal systems, and deeper reservoirs like subduction-related metamorphic fluids, or the mantle (Phillips and Powell, 2010; Tomkins, 2010; Selvaraja et al., 2017, and references therein). Moreover, the interplay between fluids and rocks, as well as ore-depositional processes, may influence the S isotope composition of $\delta^{34}S$ value (Mccuaig and Kerrich, 1998; Hodkiewicz et al., 2009). Nevertheless, we suggest a buried supracrustal unit associated with subduction-related metamorphic fluids as a reservoir of sulfur in the Kibali gold district (Tomkins, 2010; Pitcairn et al., 2021; Goldfarb and Pitcairn, 2023).

The $\delta^{34}S$ isotope compositions associated with the two ore stages in the Kibali district (i.e., py-2 and py-4) exhibit slight differences: a wide range with a negative value associated with py-2 (Fig. 11), and the heaviest $\delta^{34}S$ compositions measured in py-4b (Fig. 11). Despite the presence of a small volume of minerals reflecting oxidizing conditions like barite inclusions found adjacent to gold in the py-2 (Fig. 7b and c) and their occurrences of negative $\delta^{34}S$ values, it is improbable that oxidized fluids played a significant role during the first ore stage, given the absence of these minerals in the ore assemblage (Mccuaig and Kerrich, 1998; Adomako-Ansah et al., 2013). Instead, it is more likely that a reduced H_2S fluid evolved toward an oxidized state ^{34}S-depleted isotopic composition during the sulfidation or carbonation of the wall-rock (e.g., Palin and Xu, 2000; Adomako-Ansah et al., 2013), such as the replacement of magnetite by pyrite and siderite within the ubiquitous BIF units in the Kibali ore district.

Conversely, the second ore stage tends towards stronger ^{34}S enrichment and more positive $\delta^{34}S$ values, particularly in pyrite py-4b associated with As–Au oscillatory zoning (e.g., Chen et al., 2022). This trend can be attributed to phase separation processes (Hodkiewicz et al., 2009) resulting from fluctuations in fluid pressure (e.g., Velásquez et al., 2014; Liu et al., 2021) or may reflect fractionation when new S is deposited on the rim of a pre-existing grain. For the first alternative, pressure fluctuations likely occur during fault-valve cycles along active shear zones, as proposed by Velásquez et al. (2014). In a non-equilibrium phase separation scenario, the H_2S content within the remaining ore fluid becomes enriched in the ^{34}S isotope, leading to the formation of sulfide minerals characterized by higher $\delta^{34}S$ values (Hodkiewicz et al., 2009 and references therein).

While fluid pressure fluctuations and associated phase separation are interpreted to be the dominant control mechanisms controlling Au deposition during this event, there is a notable absence of laminae quartz vein lodes (e.g., Allibone et al., 2020), regarded as typical fault-valve features. Whereas previous authors suggest that fluid flow occurred along foliation mineral grain boundaries in relatively low permeability rocks, identification of small (mm- to cm-scale) quartz-carbonate veinlets associated with py-4b and cross-cutting the bedding may suggest the operation of an alternative mechanism driving fluid flow. Cox (2016) proposed a refined model of fault-valve behavior in the context of the injection-driven swarm, where over-pressured fluids injected into low permeability rocks induce swarm seismicity instead of the typical mainshock-aftershock pattern observed in fault-valve systems. According to this model, repeated episodes of slip, each ranging up to several centimeters, lead to an enhancement of permeability. This model may explain the presence of centimeter-scale quartz-pyrite veinlets observed in the KCD area and elucidate the hypothesis that fluctuations in fluid pressure are responsible for the phase separation and the highest δ^{34}S value observed in py-4b (Hodkiewicz et al., 2009; Meng et al., 2022). Hence, structural control emerges as a critical factor influencing the redox state of ore fluids and, consequently, the distribution of δ^{34}S values in gold-bearing pyrites in the second ore stage.

5.4. Implications for ore genesis

While the ore genesis of the Kibali gold district cannot be conclusively constrained from pyrite due to the complex history of metamorphism, deformation, and metallogenic processes (Bird, 2016; Allibone et al., 2020; Turnbull et al., 2021; Mpaka et al., 2023), the following paragraphs attempt to apply the present study to the existing geological model, illustrated in Fig. 13.

The syn-diagenetic py-0a found within the interflow volcaniclastic, basalt, and carbonaceous shale sequence in the old basin (Fig. 4) is associated with elevated trace element and Au concentrations. This early pyrite generation represents viable precursor repositories of Au, S, and variable trace elements (e.g., Large et al., 2007; Steadman et al., 2015; Steadman and Large, 2016). Under conditions of burial metamorphism to amphibolite facies, associated with deformation of the old basin, the Au and associated elements may have been released at the pyrite-pyrrhotite phase boundary (Tomkins, 2010; Goldfarb and Pitcairn, 2023) for incorporation into early hypogene gold enrichments. During a subsequent mid-orogenic extension phase between 2630 and 2625 Ma (Allibone et al., 2020), the late basin developed in which the late diagenetic to early metamorphic py-0b formed. However, this generation does not exhibit the high trace element signature in py-0a. Concomitant with sedimentation and infill of the late basin, Mpaka et al. (2023) suggest the accumulation of a placer component of detrital gold grains within the conglomeratic units of the stratigraphy. Renewed

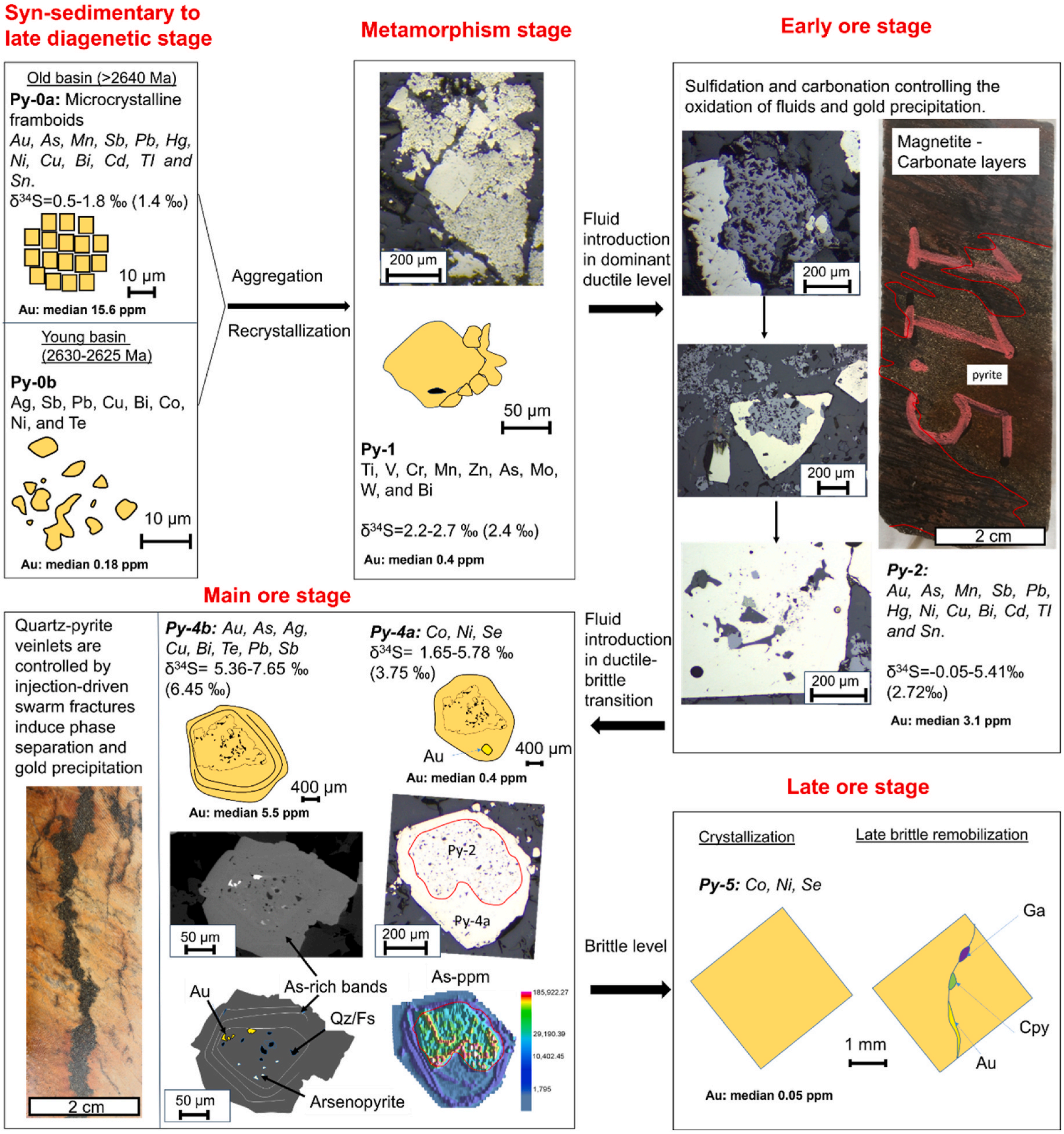

Fig. 13. Schematic diagram showing the multiple events of formation and characteristics evolution of different pyrite generations in the Kibali gold district. Abbreviation: Qz: quartz; Fs: feldspar; Ga: galena; Cpy: chalcopyrite; Py: pyrite.

collisional tectonics and associated metamorphism and deformation again promoted trace-element release from both py-0a and py-0b at metamorphic conditions relevant to the pyrite (e.g., py-1) to pyrrhotite desulfidation reaction (Zhong et al., 2015; Andersson et al., 2016; Steadman and Large, 2016; Zhao et al., 2021). The presence of abundant pyrrhotite in carbonaceous shale, graphitic rocks, basalt, and volcaniclastic rocks of the Kibali gold district supports the hypothesis that these pyrrhotite minerals originated from ancient py-0a (e.g., Schwartz, 1937; Tomkins et al., 2006; Finch and Tomkins, 2017).

The previous studies (Bird, 2016; Allibone et al., 2020) reported that the main ore stage occurs during contractional deformation due to basin inversion. Hence, they proposed that the initial barren quartz-white micas-Fe-carbonate alteration assemblage dominated by sericite and ankerite (Bird, 2016; Allibone et al., 2020) has been overprinted by later texture-destructive quartz-sericite-Fe-carbonate mineralized alteration (ankerite, siderite, pyrite, arsenopyrite, pyrrhotite, and magnetite). Based on U–Pb dating of crosscutting intrusion and detrital zircon, Allibone et al. (2020) argue that this ore-stage event occurred between 2625 and 2610 Ma. Contrary to previous claims of gold barrenness during the early alteration stage, this study suggests that the presence of py-2, characterized by the elevated presence of silicates and ankerite (Fig. 6c) relative to siderite and high amounts of trace elements, including Au, As, Bi, Cr, Cu, Gd, La, Mn, Pb, Sb, W, and Zn (Fig. 9), implies the involvement of Au-bearing fluids during this event.

The second or continued first influx of gold-bearing fluid is likely related to py-4a and py-4b emplacement, which coexist with texture-destructive alteration. The work conducted by Velásquez et al. (2014) can explain the formation of coexisting py-4a and py-4b during the ore stage carried out in El Callao. This suggests that oscillatory zoned and simple zoned pyrite can be formed by the same process but under different conditions. Zoned pyrite indicates episodic fluxes of ore fluid close to the structural conduit, whereas contemporaneous unzoned pyrite represents precipitation far away from the conduit (Velásquez et al., 2014). The abundance of zoned py-4b, associated with mm-to cm-scale quartz veinlets within sheared rocks, suggests formation related to the injection-driven swarm model (Cox, 2016; Meng et al., 2022). The over-pressured fluid flow induces fluid-pressure pulses with enhanced hydraulic fracturing in low-permeability rocks (Cox, 2016). These fluid-pressure fluctuations lead to variations in fluid chemistry and local fluid boiling, thus resulting in the oscillatory zoned pyrite with high S isotope signatures (Velásquez et al., 2014). As-rich bands are particularly amenable to hosting Au (Fig. 6d; Fig. 10), likely because of optimal surface chemistry interactions during precipitation.

Subsequent ductile deformation (S_{n+1}) experienced by the auriferous ore stage py-2 and py-4 implies localized remobilization of gold, transitioning it from invisible to visible grains next to the pyrite. This ductile remobilization created a high-grade shoot over the district, typically plunging NE. Although our understanding of the post-ore events in the Moto Greenstone Belt remains limited, there is substantial evidence of other remobilization occurring after the mineralization event and ductile deformation. This includes remobilization associated with intrusions that were emplaced between 2600 and 2530 Ma (Allibone et al., 2020; Turnbull et al., 2021), the recrystallization of pyrite during the Oubagian orogeny dated at 2 Ga (Bird, 2016); pyrite Re/Os geochronology), and reactivation during the Pan-African Orogeny, dated between 600 and 550 Ma using U/Pb monazite geochronology (Bird, 2016). The py-5 generation formed later than the main ore stage and is generally barren with respect to Au mineralization. However, in some instances (Fig. 8f), brittle fracturing of this generation provided optimal sites for accumulating late remobilized Au.

6. Conclusion

The comprehensive analysis of pyrite within the Kibali gold district has revealed a polyphase history of gold mineralization spanning the intricate record of the Moto Greenstone Belt. The application of a novel UMAP technique (detailed in the companion paper by Mpaka and von der Heyden (2024, this issue)) refined the classification of pyrite in the Kibali gold district, revealing eight distinct classes. Despite limitations in the sample size for detailed mineral chemistry through LA-ICP-MS trace element analysis and SIMS S isotope measurements, insights were extrapolated through careful examination of a broader sample set, offering a district-scale understanding.

The chemical evolution of pyrite, spanning multiple generations, was investigated, shedding light on the complex geological history of the Kibali gold district, which includes:

(1) From syn-diagenetic pyrite (py-0a) associated with early basin sequences with rich Au and trace elements, proposed as a precursor repository of gold and associated elements released during metamorphism events. This is followed by late-diagenetic to early metamorphic pyrite (py-0b) in the late basin formation to the stages of metamorphic growth (py-1), with each generation presenting unique trace element signatures and S isotopic compositions.

(2) The identification of distinct ore-stage pyrite (py-2 and py-4) where the first stage (py-2) represents the outcome of fluid-rock interactions along mineral grain boundaries within relatively impermeable rocks. These observations provide valuable insights into the mechanism of gold precipitation, accompanied by a wide range of variations and a shift to negative $\delta^{34}S$ values due to wall rock sulfidation and carbonation. The second stage (py-4) is marked by precipitation alongside quartz veinlets during the emplacement of overpressured fluid flow, inducing hydraulic fracturing, fluid chemistry variations, and phase separation.

(3) Sulfur isotopic analysis contributed to understanding the source and evolution of S in the Kibali gold district. The minimal variation in $\delta^{34}S$ values across pyrite types hinted at a single S source or homogenization during metamorphism. Variations in $\delta^{34}S$ values between ore stages (py-2 and py-4) suggested complex processes such as phase separation and pressure fluctuations influencing S isotope compositions. This latter process enriches trace elements and ^{34}S through pyrite dissolution and reprecipitation.

(4) The evolution of pyrite during deformation and remobilization provided insights into the transition from invisible gold concentrations within pyrite to visible gold precipitates. Ductile deformation processes, observed across multiple pyrite generations, played an important role in the remobilization of ore minerals. The association of deformation with gold grain formations suggested a mechanism for high-grade shoot concentration plunging NE in the district.

While the study could not conclusively define the ore genesis of the Kibali gold district, it enhances our understanding of the complex processes leading to gold mineralization and offers valuable insights for future exploration and resource assessment endeavors. With this knowledge of the isotopic signature of $\delta^{34}S$ and trace elements of pyrite, monitoring could be undertaken on a belt-wide scale to serve as an indicator for targeting. It emphasizes the crucial role played by pyrite in preserving the geological history of ore deposits and underscores the significance of adopting a holistic approach to unravel the intricacies of ore formation.

CRediT authorship contribution statement

Yann Waku Mpaka: Methodology, Investigation, Funding acquisition, Formal analysis, Data curation, Conceptualization, Project administration, Resources, Software, Visualization, Writing – original draft. **Bjorn P. Von der Heyden:** Supervision, Validation, Writing – review & editing. **Sarah Glynn:** Data curation, Methodology, Writing – review & editing. **Gary Hurst:** Writing – review & editing. **David**

Lawrence: Writing – review & editing. **Trézène Bampata:** Writing – review & editing. **Etienne Mwandale:** Writing – review & editing.

Declaration of competing interest

The authors declare the following financial interests/personal relationships which may be considered as potential competing interests: Yann Waku Mpaka reports financial support, administrative support, and equipment, drugs, or supplies were provided by Barrick Gold Corporation. Yann Waku Mpaka reports a relationship with Barrick Gold Corporation that includes: employment. Gary Hurst reports a relationship with Barrick Gold Corporation that includes: employment. David Lawrence reports a relationship with Barrick Gold Corporation that includes: employment. Trezene Bampata reports a relationship with Barrick Gold Corporation that includes: employment. Etienne Mwandale reports a relationship with Barrick Gold Corporation that includes: employment. If there are other authors, they declare that they have no known competing financial interests or personal relationships that could have appeared to influence the work reported in this paper.

Data availability

The essential data are provided in the supplementary online file.

Acknowledgements

The authors thank Barrick Gold Corporation for their financial support and for granting permission to access the data. Special recognition goes to the two anonymous reviewers and the Editor-in-Chief, Dr. Damien Delvaux, for their substantial and valuable contributions during the review process. The valuable contribution of Dr. Michael Wiedenbeck and Frédéric Couffignal in assisting with the SIMS analyses is much appreciated. Mrs. Madelaine Frazenburg, Dr. Alicia Botes, Ms. Marelize Grobbelaar, and Mrs. Riana Rossouw are acknowledged for their assistance during the SEM and LA-ICP-MS analyses. Special thanks to Dr. Francois Robert and Prof. Richard Goldfarb for their invaluable contributions in reviewing the manuscript and shaping it significantly. Thanks to the geologists, especially Fillsmith Luzolo, Esther Ndindir, Maiya Abdala and Tayi Alipi and technicians at the Kibali gold mine for their helpful assistance and constructive discussions. The authors also dedicate this work in memorial of Brou Kouakou Bernard, who made substantial contributions during the investigation but, regrettably, did not have the opportunity to witness this achievement. May he rest in peace and always remain in our hearts.

Appendix A. Supplementary data

Supplementary data to this article can be found online at https://doi.org/10.1016/j.jafrearsci.2024.105244.

References

Adomako-Ansah, K., Mizuta, T., Hammond, N.Q., Ishiyama, D., Ogata, T., Chiba, H., 2013. Gold mineralization in banded iron formation in the amalia greenstone belt, South Africa: a mineralogical and sulfur isotope study. Resour. Geol. 63, 119–140. https://doi.org/10.1111/rge.12000.

Allibone, A., Vargas, C., Mwandale, E., Kwibisa, J., Jongens, R., Quick, S., Komarnisky, N., Fanning, M., Bird, P., MacKenzie, D., Turnbull, R., Holliday, J., 2020. Chapter 9: orogenic gold deposits of the Kibali district, neoarchean moto belt, northeastern democratic republic of Congo. In: Geology of the World's Major Gold Deposits and Provinces. Society of Economic Geologists, pp. 185–201. https://doi.org/10.5382/SP.23.09.

Andersson, S.S., Jonsson, E., Högdahl, K., 2016. Metamorphism and deformation of a Palaeoproterozoic polymetallic sulphide–oxide mineralisation: hornkullen, Bergslagen, Sweden. GFF 138, 410–423. https://doi.org/10.1080/11035897.2015.1135187.

Atkinson, B.K., 1976. Deformation mechanism maps for polycrystalline galena. Earth Planet Sci. Lett. 29, 210–218. https://doi.org/10.1016/0012-821X(76)90041-8.

Augustin, J., Gaboury, D., 2019. Multi-stage and multi-sourced fluid and gold in the formation of orogenic gold deposits in the world-class Mana district of Burkina Faso – revealed by LA-ICP-MS analysis of pyrites and arsenopyrites. Ore Geol. Rev. 104, 495–521. https://doi.org/10.1016/j.oregeorev.2018.11.011.

Babedi, L., von der Heyden, B.P., Tadie, M., Mayne, M., 2022. Trace elements in pyrite from five different gold ore deposit classes: a review and meta-analysis. Geol. Soc. Lond. Spec. Publ. SP516-2021–41. https://doi.org/10.1144/sp516-2021-41.

Barker, S.L.L., Cox, S.F., 2011. Oscillatory zoning and trace element incorporation in hydrothermal minerals: insights from calcite growth experiments: REE zoning in calcite: experimental insights. Geofluids 11, 48–56. https://doi.org/10.1111/j.1468-8123.2010.00305.x.

Barker, S.L.L., Hickey, K.A., Cline, J.S., Dipple, G.M., Kilburn, M.R., Vaughan, J.R., Longo, A.A., 2009. Uncloaking invisible gold: use of nanosims to evaluate gold, trace elements, and sulfur isotopes in pyrite from carlin-type gold deposits. Econ. Geol. 104, 897–904. https://doi.org/10.2113/econgeo.104.7.897.

Barrick AIF report, 2022. Annual Information Form for the Year Ended December 31, 2022 Dated as of March 17, 2023.

Barrick report, 2022. Technical Report on the Kibali Gold Mine, Democratic Republic of the Congo.

Barrie, C.D., Boyle, A.P., Cook, N.J., Prior, D.J., 2010. Pyrite deformation textures in the massive sulfide ore deposits of the Norwegian Caledonides. Tectonophysics 483, 269–286. https://doi.org/10.1016/j.tecto.2009.10.024.

Barrie, C.D., Boyle, A.P., Salter, M., 2009. How low can you go? - extending downwards the limits of plastic deformation in pyrite. Mineral. Mag. 73, 895–913. https://doi.org/10.1180/minmag.2009.073.6.895.

Belousov, I., Large, R.R., Meffre, S., Danyushevsky, L.V., Steadman, J., Beardsmore, T., 2016. Pyrite compositions from VHMS and orogenic Au deposits in the Yilgarn Craton, Western Australia: implications for gold and copper exploration. Ore Geol. Rev. https://doi.org/10.1016/j.oregeorev.2016.04.020.

Benning, L.G., Seward, T.M., 1996. Hydrosulphide complexing of Au (I) in hydrothermal solutions from 150–400°C and 500–1500 bar. Geochem. Cosmochim. Acta 60, 1849–1871. https://doi.org/10.1016/0016-7037(96)00061-0.

Bierlein, F.P., Arne, D.C., Cartwright, I., 2004. Stable isotope (C, O, S) systematics in alteration haloes associated with orogenic gold mineralization in the Victorian gold province SE Australia. Geochem. Explor. Environ. Anal. 4, 191–211. https://doi.org/10.1144/1467-7873/04-201.

Bird, P.J., 2016. Evolution of the Kibali Granite-Greenstone Belt, North East Democratic Republic of the Congo, and Controls on Gold Mineralisation at the Kibali Gold Deposit.

Bosco-Santos, A., Gilhooly Iii, W.P., Melo-Silva, P.D., Fouskas, F., Bouyon, A., Motta, J. G., Baldim, M.R., Fabricio-Silva, W., Philippot, P., Oliveira, E.P., 2022. Neoarchean atmospheric chemistry and the preservation of S-MIF in sediments from the São Francisco Craton. Geosci. Front. 13, 101250 https://doi.org/10.1016/j.gsf.2021.101250.

Brueckner, S.M., Kline, A.K., Bilenker, L.D., Poole, J., Whitney, M.S., 2021. Mineral chemistry and sulfur isotope geochemistry from tonalite-hosted, gold-bearing quartz veins at hog mountain, southwestern appalachians: implications for gold precipitation mechanism, sulfur source, and genesis. Econ. Geol. 116, 357–388. https://doi.org/10.5382/econgeo.4786.

Chang, J., Li, Y., Lu, H., 2022. The morphological characteristics of authigenic pyrite formed in marine sediments. J. Mar. Sci. Eng. 10, 1533. https://doi.org/10.3390/jmse10101533.

Chang, Z., Large, R.R., Maslennikov, V., 2008. Sulfur isotopes in sediment-hosted orogenic gold deposits: evidence for an early timing and a seawater sulfur source. Geology 36, 971. https://doi.org/10.1130/G25001A.1.

Chen, X., Wu, Y., Zhou, K., Zheng, Y., Xiao, F., Wang, Y., 2022. Fluid inclusion and in situ sulfur isotope studies of the carbonaceous strata-hosted Eryiling gold deposit in the Beishan orogen, NW China. Ore Geol. Rev. 149, 105099 https://doi.org/10.1016/j.oregeorev.2022.105099.

Chouinard, A., Paquette, J., Williams-Jones, A.E., 2005. Crystallographic controls on trace-element incorporation in Auriferous pyrite from the Pascua epithermal high-sulfidation deposit, Chile-Argentina. Can. Mineral. 43, 951–963. https://doi.org/10.2113/gscanmin.43.3.951.

Chowdhury, S., Pal, D.C., Papineau, D., Lentz, D.R., 2020. Major and trace element and multiple sulfur isotope composition of sulfides from the Paleoproterozoic Surda copper deposit, Singhbhum shear Zone, India: implications for the mineralization processes. Ore Geol. Rev. 120 https://doi.org/10.1016/j.oregeorev.2020.103396.

Ciobanu, C.L., Cook, N.J., Pring, A., Brugger, J., Danyushevsky, L.V., Shimizu, M., 2009. 'Invisible gold' in bismuth chalcogenides. Geochem. Cosmochim. Acta 73, 1970–1999. https://doi.org/10.1016/j.gca.2009.01.006.

Conn, C.D., Spry, P.G., Layton-Matthews, D., Voinot, A., Koenig, A., 2019. The effects of amphibolite facies metamorphism on the trace element composition of pyrite and pyrrhotite in the Cambrian Nairne Pyrite Member, Kanmantoo Group, South Australia. Ore Geol. Rev. 114 https://doi.org/10.1016/j.oregeorev.2019.103128.

Cook, N.J., Ciobanu, C.L., Mao, J., 2009. Textural control on gold distribution in as-free pyrite from the dongping, huangtuliang and hougou gold deposits, north China Craton (hebei province, China). Chem. Geol. 264, 101–121. https://doi.org/10.1016/j.chemgeo.2009.02.020.

Cook, N.J., Ciobanu, C.L., Meria, D., Silcock, D., Wade, B., 2013. Arsenopyrite-pyrite association in an orogenic gold ore: tracing mineralization history from textures and trace elements. Econ. Geol. 108, 1273–1283. https://doi.org/10.2113/econgeo.108.6.1273.

Cox, S.F., 2016. Injection-driven swarm seismicity and permeability enhancement: implications for the dynamics of hydrothermal ore systems in high fluid-flux, overpressured faulting regimes—an invited paper. Econ. Geol. 111, 559–587. https://doi.org/10.2113/econgeo.111.3.559.

Cox, S.F., 1987. Antitaxial crack-seal vein microstructures and their relationship to displacement paths. J. Struct. Geol. 9, 779–787. https://doi.org/10.1016/0191-8141(87)90079-4.

Cox, S.F., Etheridge, M.A., Hobbs, B.E., 1981. The experimental ductile deformation of polycrystalline and single crystal pyrite. Econ. Geol. 76, 2105–2117. https://doi.org/10.2113/gsecongeo.76.8.2105.

Crowe, D.E., Vaughan, R.G., 1996. Characterization and use of isotopically homogeneous standards for in situ laser microprobe analysis of ^{34} S/^{32} S ratios. Am. Mineral. 81, 187–193. https://doi.org/10.2138/am-1996-1-223.

Deditius, A.P., Utsunomiya, S., Reich, M., Kesler, S.E., Ewing, R.C., Hough, R., Walshe, J., 2011. Trace metal nanoparticles in pyrite. Ore Geol. Rev. 42, 32–46. https://doi.org/10.1016/j.oregeorev.2011.03.003.

Deditius, A.P., Utsunomiya, S., Renock, D., Ewing, R.C., Ramana, C.V., Becker, U., Kesler, S.E., 2008. A proposed new type of arsenian pyrite: composition, nanostructure and geological significance. Geochem. Cosmochim. Acta 72, 2919–2933. https://doi.org/10.1016/j.gca.2008.03.014.

Ding, T., Valkiers, S., Kipphardt, H., De Bièvre, P., Taylor, P.D.P., Gonfiantini, R., Krouse, R., 2001. Calibrated sulfur isotope abundance ratios of three IAEA sulfur isotope reference materials and V-CDT with a reassessment of the atomic weight of sulfur. Geochem. Cosmochim. Acta 65, 2433–2437. https://doi.org/10.1016/S0016-7037(01)00611-1.

Dmitrijeva, M., Cook, N.J., Ehrig, K., Ciobanu, C.L., Metcalfe, A.V., Kamenetsky, M., Kamenetsky, V.S., Gilbert, S., 2020. Multivariate statistical analysis of trace elements in pyrite: prediction, bias and artefacts in defining mineral signatures. Minerals 10. https://doi.org/10.3390/min10010061.

Du, R., Xian, H., Wu, X., Zhu, J., Wei, J., Xing, J., Tan, W., He, H., 2021. Morphology dominated rapid oxidation of framboidal pyrite. Geochem. Perspect. Lett. 16, 53–58. https://doi.org/10.7185/geochemlet.2104.

Feng, Y., Zhang, Y., Xie, Y., Shao, Y., Lai, C., 2020. Pyrite geochemistry and metallogenic implications of gutaishan Au deposit in jiangnan orogen, South China. Ore Geol. Rev. 117, 103298 https://doi.org/10.1016/j.oregeorev.2019.103298.

Fike, D.A., Bradley, A.S., Rose, C.V., 2015. Rethinking the ancient sulfur cycle. Annu. Rev. Earth Planet Sci. 43, 593–622. https://doi.org/10.1146/annurev-earth-060313-054802.

Filimonova, O.N., Tagirov, B.R., Trigub, A.L., Nickolsky, M.S., Rovezzi, M., Belogub, E. V., Reukov, V.L., Vikentyev, I.V., 2020. The state of Au and as in pyrite studied by X-ray absorption spectroscopy of natural minerals and synthetic phases. Ore Geol. Rev. 121, 103475 https://doi.org/10.1016/j.oregeorev.2020.103475.

Finch, E.G., Tomkins, A.G., 2017. Pyrite-pyrrhotite stability in a metamorphic aureole: implications for orogenic gold genesis. Econ. Geol. 112, 661–674. https://doi.org/10.2113/econgeo.112.3.661.

Fischer, W.W., Fike, D.A., Johnson, J.E., Raub, T.D., Guan, Y., Kirschvink, J.L., Eiler, J. M., 2014. SQUID–SIMS is a useful approach to uncover primary signals in the Archean sulfur cycle. Proc. Natl. Acad. Sci. USA 111, 5468–5473. https://doi.org/10.1073/pnas.1322577111.

Fleet, M.E., Mumin, A.H., 1997. Gold-bearing arsenian pyrite and marcasite and arsenopyrite from Carlin Trend gold deposits and laboratory synthesis. Am. Mineral.

Fleming, R.H., Bekken, B.M., 1995. Isotope ratio and trace element imaging of pyrite grains in gold ores. Int. J. Mass Spectrom. Ion Process. 143, 213–224. https://doi.org/10.1016/0168-1176(94)04138-W.

Fougerouse, D., Micklethwaite, S., Tomkins, A.G., Mei, Y., Kilburn, M., Guagliardo, P., Fisher, L.A., Halfpenny, A., Gee, M., Paterson, D., Howard, D.L., 2016. Gold remobilisation and formation of high grade ore shoots driven by dissolution-reprecipitation replacement and Ni substitution into auriferous arsenopyrite. Geochem. Cosmochim. Acta 178, 143–159. https://doi.org/10.1016/j.gca.2016.01.040.

George, L.L., Biagioni, C., D'Orazio, M., Cook, N.J., 2018. Textural and trace element evolution of pyrite during greenschist facies metamorphic recrystallization in the southern Apuan Alps (Tuscany, Italy): influence on the formation of Tl-rich sulfosalt melt. Ore Geol. Rev. 102, 59–105. https://doi.org/10.1016/j.oregeorev.2018.08.032.

Goldfarb, R.J., Groves, D.I., 2015. Orogenic gold: common or evolving fluid and metal sources through time. Lithos. https://doi.org/10.1016/j.lithos.2015.07.011.

Goldfarb, R.J., Pitcairn, I., 2023. Orogenic gold: is a genetic association with magmatism realistic? Miner. Deposita 58, 5–35. https://doi.org/10.1007/s00126-022-01146-8.

Gregory, D.D., Cracknell, M.J., Large, R.R., McGoldrick, P., Kuhn, S., Maslennikov, V.V., Baker, M.J., Fox, N., Belousov, I., Figueroa, M.C., Steadman, J.A., Fabris, A.J., Lyons, T.W., 2019. Distinguishing ore deposit type and barren sedimentary pyrite using laser ablation-inductively coupled plasma-mass spectrometry trace element data and statistical analysis of large data sets. Econ. Geol. 114, 771–786. https://doi.org/10.5382/econgeo.4654.

Gregory, D.D., Large, R.R., Halpin, J.A., Baturina, E.L., Lyons, T.W., Wu, S., Danyushevsky, L., Sack, P.J., Chappaz, A., Maslennikov, V.V., Bull, S.W., 2015. Trace element content of sedimentary pyrite in black shales. Econ. Geol. 110, 1389–1410. https://doi.org/10.2113/econgeo.110.6.1389.

Hastie, E.C.G., Kontak, D.J., Lafrance, B., 2020. Gold remobilization: insights from gold deposits in the archean Swayze greenstone belt, abitibi subprovince, Canada. Econ. Geol. 115, 241–277. https://doi.org/10.5382/ECONGEO.4709.

Hayashi, K., Ohmoto, H., 1991. Solubility of gold in NaCl-and H2S-bearing aqueous solutions at 250–350°C. Geochem. Cosmochim. Acta 55, 2111–2126. https://doi.org/10.1016/0016-7037(91)90091-I.

Hodkiewicz, P.F., Groves, D.I., Davidson, G.J., Weinberg, R.F., Hagemann, S.G., 2009. Influence of structural setting on sulphur isotopes in Archean orogenic gold deposits, Eastern Goldfields Province, Yilgarn, Western Australia. Miner. Deposita 44, 129–150. https://doi.org/10.1007/s00126-008-0211-5.

Jochum, K.P., Nohl, U., Herwig, K., Lammel, E., Stoll, B., Hofmann, A.W., 2005. GeoReM: a new geochemical database for reference materials and isotopic standards. Geostand. Geoanal. Res. 29, 333–338. https://doi.org/10.1111/j.1751-908X.2005.tb00904.x.

Jochum, K.P., Weis, U., Schwager, B., Stoll, B., Wilson, S.A., Haug, G.H., Andreae, M.O., Enzweiler, J., 2016. Reference values following ISO guidelines for frequently requested rock reference materials. Geostand. Geoanal. Res. 40, 333–350. https://doi.org/10.1111/j.1751-908X.2015.00392.x.

Kampmann, T.C., Jansson, N.F., Stephens, M.B., Olin, P.H., Gilbert, S., Wanhainen, C., 2018. Syn-tectonic sulphide remobilization and trace element redistribution at the Falun pyritic Zn-Pb-Cu-(Au-Ag) sulphide deposit, Bergslagen, Sweden. Ore Geol. Rev. 96, 48–71. https://doi.org/10.1016/j.oregeorev.2018.04.010.

Kattenhorn, S.A., 1994. Mechanisms of Sill and Dyke Intrusion.

Keith, M., Smith, D.J., Jenkin, G.R.T., Holwell, D.A., Dye, M.D., 2018. A review of Te and Se systematics in hydrothermal pyrite from precious metal deposits: insights into ore-forming processes. Ore Geol. Rev. https://doi.org/10.1016/j.oregeorev.2017.07.023.

Kusebauch, C., Oelze, M., Gleeson, S.A., 2018. Partitioning of arsenic between hydrothermal fluid and pyrite during experimental siderite replacement. Chem. Geol. 500, 136–147. https://doi.org/10.1016/j.chemgeo.2018.09.027.

Large, R.R., Danyushevsky, L., Hollit, C., Maslennikov, V., Meffre, S., Gilbert, S., Bull, S., Scott, R., Emsbo, P., Thomas, H., Singh, B., Foster, J., 2009. Gold and trace element zonation in pyrite using a laser imaging technique: implications for the timing of gold in orogenic and carlin-style sediment-hosted deposits. Econ. Geol. 104, 635–668. https://doi.org/10.2113/gsecongeo.104.5.635.

Large, R.R., Halpin, J.A., Danyushevsky, L.V., Maslennikov, V.V., Bull, S.W., Long, J.A., Gregory, D.D., Lounejeva, E., Lyons, T.W., Sack, P.J., McGoldrick, P.J., Calver, C.R., 2014. Trace element content of sedimentary pyrite as a new proxy for deep-time ocean–atmosphere evolution. Earth Planet Sci. Lett. 389, 209–220. https://doi.org/10.1016/j.epsl.2013.12.020.

Large, R.R., Maslennikov, V.V., Robert, F., Danyushevsky, L.V., Chang, Z., 2007. Multistage sedimentary and metamorphic origin of pyrite and gold in the giant sukhoi log deposit, lena gold province, Russia. Econ. Geol. 102, 1233–1267. https://doi.org/10.2113/gsecongeo.102.7.1233.

Lavreau, J., 1984. Vein and stratabound gold deposits of northern Zaire. Miner. Deposita 19. https://doi.org/10.1007/BF00204680.

Lawrence, D.M., Treloar, P.J., Rankin, A.H., Boyce, A., Harbidge, P., 2013. A fluid inclusion and stable isotope study at the loulo mining district, Mali, west Africa: implications for multifluid sources in the generation of orogenic gold deposits. Econ. Geol. 108, 229–257. https://doi.org/10.2113/econgeo.108.2.229.

Leach, A.M., Hieftje, G.M., 2000. Methods for shot-to-shot normalization in laser ablation with an inductively coupled plasma time-of-flight mass spectrometer. J. Anal. At. Spectrom. 15, 1121–1124. https://doi.org/10.1039/b001968m.

Li, J., Yang, Z., Song, M., Dong, L., Li, S., Wang, R., Liu, X., Li, Z., Song, Y., Lai, C., 2023. Gold remobilization of the Sanshandao gold deposit, Jiaodong Peninsula, Eastern China: perspective from in-situ sulfide trace elements and sulfur isotopes. Ore Geol. Rev. 158, 105505 https://doi.org/10.1016/j.oregeorev.2023.105505.

Li, J., Zhang, Z., Stern, R.A., Hannah, J.L., Stein, H.J., Yang, G., Li, L., 2017. Primary multiple sulfur isotopic compositions of pyrite in 2.7 Ga shales from the Joy Lake sequence (Superior Province) show felsic volcanic array-like signature. Geochem. Cosmochim. Acta 202, 310–340. https://doi.org/10.1016/j.gca.2016.12.037.

Li, N., Deng, J., Groves, D.I., Han, R., 2019. Controls on the distribution of invisible and visible gold in the orogenic gold deposits of the Yangshan Gold Belt, West Qinling Orogen, China. Minerals 9. https://doi.org/10.3390/min9020092.

Li, R., Chen, H., Large, R.R., Zhao, L., Liu, Y., Jiao, J., Xia, X.P., Yang, Q., 2020. Ore-forming fluid source of the orogenic gold deposit: implications from a combined pyrite texture and geochemistry study. Chem. Geol. 552 https://doi.org/10.1016/j.chemgeo.2020.119781.

Li, W., Cook, N.J., Xie, G.-Q., Mao, J.-W., Ciobanu, C.L., Fu, B., 2021. Complementary textural, trace element, and isotopic analyses of sulfides constrain ore-forming processes for the slate-hosted Yuhengtang Au deposit, South China. Econ. Geol. 116, 1825–1848. https://doi.org/10.5382/econgeo.4847.

Lipko, S., Tauson, V., Smagunov, N., Babkin, D., Parkhomenko, I., 2022. Distribution of trace elements (Ag, Pd, Cd, and Mn) between pyrite and pyrrhotite and selectivity of surficial nonautonomous phases in a hydrothermal system. Minerals 12, 1165. https://doi.org/10.3390/min12091165.

Liu, L., Ireland, T.R., Holden, P., Ávila, J., Vasconcelos, P., Mavrogenes, J., 2021. Sources of auriferous fluids associated with a Neoarchean BIF-hosted orogenic gold deposit revealed by the multiple sulfur isotopic compositions of zoned pyrites. Contrib. Mineral. Petrol. 176 https://doi.org/10.1007/s00410-021-01788-3.

Ma, Y., Jiang, S.Y., Frimmel, H.E., 2022. Deciphering multiple ore-forming processes of the Shuangqishan orogenic gold deposit, Southeast China by in situ analysis of pyrite. Ore Geol. Rev. 142 https://doi.org/10.1016/j.oregeorev.2022.104730.

Maddox, L.M., Bancroft, G.M., Scaini, M.J., Lorimer, J.W., 1998. Invisible gold; comparison of Au deposition on pyrite and arsenopyrite. Am. Mineral. 83, 1240–1245. https://doi.org/10.2138/am-1998-11-1212.

Majumdar, S., Singh, S., Sahoo, P.R., Venkatesh, A.S., 2019. Trace-element systematics of pyrite and its implications for refractory gold mineralisation within the carbonaceous metasedimentary units of Palaeoproterozoic South Purulia shear zone, eastern India. J. Earth Syst. Sci. 128 https://doi.org/10.1007/s12040-019-1256-9.

Marshall, B., Gilligan, L.B., 1993. Remobilization, syn-tectonic processes and massive sulphide deposits. Ore Geol. Rev. 8, 39–64. https://doi.org/10.1016/0169-1368(93)90027-V.

Marshall, B., Gilligan, L.B., 1987. An introduction to remobilization: information from ore-body geometry and experimental considerations. Ore Geol. Rev. 2, 87–131. https://doi.org/10.1016/0169-1368(87)90025-4.

Marshall, B., Vokes, F.M., Spry, P.G., 1998. Regional metamorphic remobilization: upgrading and formation of ore deposits. In: Metamorphic and Metamorphogenic Ore Deposits. Society of Economic Geologists, pp. 19–38. https://doi.org/10.5382/Rev.11.02.

Maslennikov, V.V., Maslennikova, S.P., Large, R.R., Danyushevsky, L.V., 2009. Study of trace element zonation in vent chimneys from the silurian yaman-kasy volcanic-hosted massive sulfide deposit (southern urals, Russia) using laser ablation-inductively coupled plasma mass spectrometry (LA-ICPMS). Econ. Geol. 104, 1111–1141. https://doi.org/10.2113/gsecongeo.104.8.1111.

Mathieu, L., 2019. Detecting magmatic-derived fluids using pyrite chemistry: example of the Chibougamau area, Abitibi Subprovince, Québec. Ore Geol. Rev. https://doi.org/10.1016/j.oregeorev.2019.103127.

Maurer, V.C., Melo, G.H.C. de, Lana, C. de C., Marinho, M. de S., Batista, S.P.V., Silveira, L.M. da, Queiroga, G., Castro, M.P., Silva, M., 2021. Trace elements in pyrite and pyrrhotite in the Pitangui Orogenic Au deposit, Pitangui greenstone belt, São Francisco Craton: implications for the ore-forming fluids and metal sources. J. South Am. Earth Sci. 111 https://doi.org/10.1016/j.jsames.2021.103459.

McClay, K.R., Ellis, P.G., 1983. Deformation and recrystallization of pyrite. Mineral. Mag. 47, 527–538. https://doi.org/10.1180/minmag.1983.047.345.14.

Mccuaig, T.C., Kerrich, R., 1998. P-T-t-deformation-fluid characteristics of lode gold deposits: evidence from alteration systematics. C McCuaig R Kerrich Ore Geol. Rev.

Meng, L., Huang, F., Gao, W., Wang, D., Zhu, J., Xing, C., Tan, W., Tang, X., 2020. Multi-stage hydrothermal processes at the Laozuoshan gold deposit in NE China: insights from textures and compositions of sulfide assemblages. Ore Geol. Rev. 117, 103275 https://doi.org/10.1016/j.oregeorev.2019.103275.

Meng, L., Lan, C., Zhan, Q., Wu, Q., Zhao, T., 2022. Origin of the Shanggong gold deposit, the southern margin of the North China Craton: constraints from Rb-Sr ages of sericite, and trace elements and sulfur isotope of pyrite. Ore Geol. Rev. 142 https://doi.org/10.1016/j.oregeorev.2022.104728.

Meyer, N.R., Zerkle, A.L., Fike, D.A., 2017. Sulphur cycling in a Neoarchaean microbial mat. Geobiology 15, 353–365. https://doi.org/10.1111/gbi.12227.

Mpaka, Y.W., von der Heyden, B.P., Lawrence, D., Bampata, T., Ndongani, F.L., Mwandale, E., 2023. A paleoplacer component to the gold hosted in meta-conglomeratic units of the Neoarchaean moto greenstone belt. DRC. Ore Geol. Rev. 157 https://doi.org/10.1016/j.oregeorev.2023.105477.

Mpaka, Y.W., von der Heyden, B.P., 2023. this issue. Enhanced Classification of Pyrite Generations Based on Mineral Chemistry Using Uniform Manifold Approximation and Projection (UMAP).

Norris L., Danyushevsky A., 2018. Towards Estimating the Complete Uncertainty Budget of Quantified Results Measured by LA-ICP-MS, Goldschmidt, Boston.

Ohmoto, H., 1972. Systematics of sulfur and carbon isotopes in hydrothermal ore deposits. Econ. Geol. 67, 551–578. https://doi.org/10.2113/gsecongeo.67.5.551.

Ohmoto, H., Goldhaber, M.B., 1997. Sulfur and carbon isotopes. In: Geochemistry of Hydrothermal Ore Deposits. HL Barnes.

Palin, J.M., Xu, Y., 2000. Gilt by association? Origins of pyritic gold ores in theVictory mesothermal gold deposit, western Australia. Econ. Geol. 95, 1627–1634. https://doi.org/10.2113/gsecongeo.95.8.1627.

Perret, J., André-Mayer, A.-S., Eglinger, A., Feneyrol, J., Voinot, A., Morlot, C., Barou, F., Teitler, Y., Seira, D., Bosc, R., 2022. Structural and geochemical ore-forming processes in deformed gold deposits: towards a multiscale and multimethod approach. Geol. Soc. Lond. Spec. Publ. 516, 211–242. https://doi.org/10.1144/SP516-2021-37.

Perret, J., Eglinger, A., André-Mayer, A.-S., Aillères, L., Feneyrol, J., Hartshorne, C., Abanyin, E., Bosc, R., 2020. Subvertical, linear and progressive deformation related to gold mineralization at the Galat Sufar South deposit, Nubian Shield, NE Sudan. J. Struct. Geol. 135, 104032 https://doi.org/10.1016/j.jsg.2020.104032.

Peterson, E.C., Mavrogenes, J., 2014. Linking high-grade gold mineralization to earthquake-induced fault-valve processes in the Porgera gold deposit, Papua New Guinea. Geology 42, 383–386. https://doi.org/10.1130/g35286.1.

Phillips, G.N., Groves, D.I., Neall, F.B., Donnelly, T.H., Lambert, I.B., 1986. Anomalous sulfur isotope compositions in the Golden Mile. Kalgoorlie. Econ. Geol. 81, 2008–2015. https://doi.org/10.2113/gsecongeo.81.8.2008.

Phillips, G.N., Powell, R., 2010. Formation of gold deposits: a metamorphic devolatilization model. J. Metamorph. Geol. 28, 689–718. https://doi.org/10.1111/j.1525-1314.2010.00887.x.

Phillips, N., 2022. Formation of Gold Deposits. Springer Nature, Singapore. https://doi.org/10.1007/978-981-16-3081-1.

Pitcairn, I.K., Leventis, N., Beaudoin, G., Faure, S., Guilmette, C., Dubé, B., 2021. A metasedimentary source of gold in archean orogenic gold deposits. Geology 49, 862–866. https://doi.org/10.1130/G48587.1.

Pokrovski, G.S., Escoda, C., Blanchard, M., Testemale, D., Hazemann, J.L., Gouy, S., Kokh, M.A., Boiron, M.C., Parseval, F.D., Aigouy, T., Menjot, L., Parseval, P.D., Proux, O., Rovezzi, M., Béziat, D., Salvi, S., Kouzmanov, K., Bartsch, T., Pöttgen, R., Doert, T., 2021. An arsenic-driven pump for invisible gold in hydrothermal systems. Geochem. Perspect. Lett. 17, 39–44. https://doi.org/10.7185/geochemlet.2112.

Pokrovski, G.S., Kara, S., Roux, J., 2002. Stability and solubility of arsenopyrite, FeAsS, in crustal fluids. Geochem. Cosmochim. Acta 66, 2361–2378. https://doi.org/10.1016/S0016-7037(02)00836-0.

Pokrovski, G.S., Kokh, M.A., Proux, O., Hazemann, J.-L., Bazarkina, E.F., Testemale, D., Escoda, C., Boiron, M.-C., Blanchard, M., Aigouy, T., Gouy, S., De Parseval, P., Thibaut, M., 2019. The nature and partitioning of invisible gold in the pyrite-fluid system. Ore Geol. Rev. 109, 545–563. https://doi.org/10.1016/j.oregeorev.2019.04.024.

Qian, G., Xia, F., Brugger, J., Skinner, W.M., Bei, J., Chen, G., Pring, A., 2011. Replacement of pyrrhotite by pyrite and marcasite under hydrothermal conditions up to 220 °C: an experimental study of reaction textures and mechanisms. Am. Mineral. 96, 1878–1893. https://doi.org/10.2138/am.2011.3691.

Raič, S., Molnár, F., Cook, N., O'Brien, H., Lahaye, Y., 2022. Application of lithogeochemical and pyrite trace element data for the determination of vectors to ore in the Raja Au-Co prospect, northern Finland. Solid Earth 13, 271–299. https://doi.org/10.5194/se-13-271-2022.

Rajabpour, S., Behzadi, M., Jiang, S.-Y., Rasa, I., Lehmann, B., Ma, Y., 2017. Sulfide chemistry and sulfur isotope characteristics of the Cenozoic volcanic-hosted Kuh-Pang copper deposit, Saveh county, northwestern central Iran. Ore Geol. Rev. 86, 563–583. https://doi.org/10.1016/j.oregeorev.2017.03.001.

Reich, M., Deditius, A., Chryssoulis, S., Li, J.W., Ma, C.Q., Parada, M.A., Barra, F., Mittermayr, F., 2013. Pyrite as a record of hydrothermal fluid evolution in a porphyry copper system: a SIMS/EMPA trace element study. Geochem. Cosmochim. Acta 104, 42–62. https://doi.org/10.1016/j.gca.2012.11.006.

Reich, M., Kesler, S.E., Utsunomiya, S., Palenik, C.S., Chryssoulis, S.L., Ewing, R.C., 2005. Solubility of gold in arsenian pyrite. Geochem. Cosmochim. Acta 69, 2781–2796. https://doi.org/10.1016/j.gca.2005.01.011.

Rieger, P., Magnall, J.M., Gleeson, S.A., Oelze, M., 2023. Pyrite chemistry records a multistage ore forming system at the Proterozoic George Fisher massive sulfide Zn-Pb-Ag deposit, Mount Isa, Australia. Front. Earth Sci. 11 https://doi.org/10.3389/feart.2023.892759.

Rollinson, 1993. Using Geochemical Data : Evaluation, Presentation, Interpretation. Longman Scientific and Technical, England.

Román, N., Reich, M., Leisen, M., Morata, D., Barra, F., Deditius, A.P., 2019. Geochemical and micro-textural fingerprints of boiling in pyrite. Geochem. Cosmochim. Acta 246, 60–85. https://doi.org/10.1016/J.GCA.2018.11.034.

Schwartz, G.M., 1937. The paragenesis of pyrrhotite. Econ. Geol. 32, 31–55. https://doi.org/10.2113/gsecongeo.32.1.31.

Seal, R.R., 2006. Sulfur isotope geochemistry of sulfide minerals. Rev. Mineral. Geochem. 61, 633–677. https://doi.org/10.2138/rmg.2006.61.12.

Selvaraja, V., Fiorentini, M.L., Jeon, H., Savard, D.D., LaFlamme, C.K., Guagliardo, P., Caruso, S., Bui, T.H., 2017. Evidence of local sourcing of sulfur and gold in an Archaean sediment-hosted gold deposit. Ore Geol. Rev. 89, 909–930. https://doi.org/10.1016/j.oregeorev.2017.07.021.

Simon, G., Huang, H., Penner-Hahn, J.E., Kesler, S.E., Kao, L.-S., 1999. Oxidation state of gold and arsenic in gold-bearing arsenian pyrite. Am. Mineral. 84, 1071–1079. https://doi.org/10.2138/am-1999-7-809.

Steadman, J.A., Large, R.R., 2016. Synsedimentary, diagenetic, and metamorphic pyrite, pyrrhotite, and marcasite at the homestake BIF-hosted gold deposit, South Dakota, USA: insights on Au-as ore genesis from textural and LA-ICP-MS trace element studies. Econ. Geol. 111, 1731–1752. https://doi.org/10.2113/econgeo.111.7.1731.

Steadman, J.A., Large, R.R., Blamey, N.J., Mukherjee, I., Corkrey, R., Danyushevsky, L.V., Maslennikov, V., Hollings, P., Garven, G., Brand, U., Lécuyer, C., 2020. Evidence for elevated and variable atmospheric oxygen in the Precambrian. Precambrian Res. 343, 105722 https://doi.org/10.1016/j.precamres.2020.105722.

Steadman, J.A., Large, R.R., Meffre, S., Olin, P.H., Danyushevsky, L.V., Gregory, D.D., Belousov, I., Lounejeva, E., Ireland, T.R., Holden, P., 2015. Synsedimentary to early diagenetic gold in black shale-hosted pyrite nodules at the golden mile deposit, Kalgoorlie, western Australia. Econ. Geol. 110, 1157–1191. https://doi.org/10.2113/econgeo.110.5.1157.

Steadman, J.A., Large, R.R., Olin, P.H., Danyushevsky, L.V., Meffre, S., Huston, D., Fabris, A., Lisitsin, V., Wells, T., 2021. Pyrite trace element behavior in magmatic-hydrothermal environments: an LA-ICPMS imaging study. Ore Geol. Rev. https://doi.org/10.1016/j.oregeorev.2020.103878.

Stefánsson, A., Seward, T.M., 2004. Gold(I) complexing in aqueous sulphide solutions to 500°C at 500 bar. Geochem. Cosmochim. Acta 68, 4121–4143. https://doi.org/10.1016/j.gca.2004.04.006.

Su, Z.-K., Zhao, X.-F., Wang, C.Y., 2023. Trace elements and sulfur isotopic compositions of sulfides in the giant Dahongshan Fe-Cu-(Au-Co) deposit, SW China: implications for fluid evolution and Co enrichment in IOCG systems. Ore Geol. Rev. 157, 105401 https://doi.org/10.1016/j.oregeorev.2023.105401.

Sun, G., Zeng, Q., Zhou, L., Wang, Y., Chen, P., 2020. Trace element contents and in situ sulfur isotope analyses of pyrite in the Baiyun gold deposit, NE China: implication for the genesis of intrusion-related gold deposits. Ore Geol. Rev. 118 https://doi.org/10.1016/j.oregeorev.2020.103330.

Sung, Y.H., Brugger, J., Ciobanu, C.L., Pring, A., Skinner, W., Nugus, M., 2009. Invisible gold in arsenian pyrite and arsenopyrite from a multistage archaean gold deposit: sunrise dam, eastern goldfields province, western Australia. Miner. Deposita 44, 765–791. https://doi.org/10.1007/s00126-009-0244-4.

Tan, H., Shao, Y., Liu, Q., Zhang, Yu, Feng, Y., Zhang, Yuce, Shah, S.A., 2022. Textures, trace element geochemistry and in-situ sulfur isotopes of pyrite from the Xiaojiashan gold deposit, Jiangnan Orogen: implications for ore genesis. Ore Geol. Rev. 144 https://doi.org/10.1016/j.oregeorev.2022.104843.

Tomkins, A.G., 2010. Windows of metamorphic sulfur liberation in the crust: implications for gold deposit genesis. Geochem. Cosmochim. Acta 74, 3246–3259. https://doi.org/10.1016/j.gca.2010.03.003.

Tomkins, A.G., 2007. Three mechanisms of ore re-mobilisation during amphibolite facies metamorphism at the Montauban Zn–Pb–Au–Ag deposit. Miner. Deposita 42, 627–637. https://doi.org/10.1007/s00126-007-0131-9.

Tomkins, A.G., Frost, B.R., Pattison, D.R.M., 2006. Arsenopyrite melting during metamorphism of sulfide ore deposits. Can. Mineral. 44, 1045–1062.

Turnbull, R.E., Allibone, A.H., Matheys, F., Fanning, C.M., Kasereka, E., Kabete, J., McNaughton, N.J., Mwandale, E., Holliday, J., 2021. Geology and geochronology of the Archean plutonic rocks in the northeast Democratic Republic of Congo. Precambrian Res. 358, 106133 https://doi.org/10.1016/j.precamres.2021.106133.

Vaughan, J.P., Kyin, A., 2004. Refractory gold ores in Archaean greenstones,Western Australia: mineralogy, gold paragenesis, metallurgical characterization and classification. Mineral. Mag. 68, 255–277. https://doi.org/10.1180/0026461046820186.

Velásquez, G., Béziat, D., Salvi, S., Siebenaller, L., Borisova, A.Y., Pokrovski, G.S., Parseval, P.D., 2014. Formation and deformation of pyrite and implications for gold mineralization in the El Callao District, Venezuela. Econ. Geol. 109, 457–486. https://doi.org/10.2113/econgeo.109.2.457.

Voisey, C.R., Willis, D., Tomkins, A.G., Wilson, C.J.L., Micklethwaite, S., Salvemini, F., Bougoure, J., Rickard, W.D.A., 2020. Aseismic refinement of orogenic gold systems. Econ. Geol. 115, 33–50. https://doi.org/10.5382/econgeo.4692.

Wacey, D., McLoughlin, N., Whitehouse, M.J., Kilburn, M.R., 2010. Two coexisting sulfur metabolisms in a ca. 3400 Ma sandstone. Geology 38, 1115–1118. https://doi.org/10.1130/G31329.1.

Walker, A.T., Evans, K.A., Kirkland, C.L., 2020. A novel application of image analysis to interpret trace element distributions in magmatic sulphides. Lithos 362–363, 105451. https://doi.org/10.1016/j.lithos.2020.105451.

Wang, X., Shi, M., Zhang, J., Pang, Y., Zhao, Y., 2021. Significance of trace elements in marine shale pyrite for reconstructing the sedimentary environment: a case study of niutitang and hongshuizhuang formations. ACS Earth Space Chem. 5, 3210–3225. https://doi.org/10.1021/acsearthspacechem.1c00280.

Wei, D., Zhou, Tao-Fa, Xia, Yong, Chen, J., Xie, Z., Liu, X., Pang, Bao-Cheng, Tan, Q., Bai, Ling-An, 2022. Ore fluid origin recorded by apatite chemistry: a case study on altered dolerite from the Badu Carlin-type gold deposit, Youjiang basin, SW China. Ore Geol. Rev., 104745 https://doi.org/10.1016/j.oregeorev.2022.104745.

Williams-Jones, A.E., Bowell, R.J., Migdisov, A.A., 2009. Gold in solution. Elements 5, 281–287. https://doi.org/10.2113/gselements.5.5.281.

Winderbaum, L., Ciobanu, C.L., Cook, N.J., Paul, M., Metcalfe, A., Gilbert, S., 2012. Multivariate analysis of an LA-ICP-MS trace element dataset for pyrite. Math. Geosci. 44, 823–842. https://doi.org/10.1007/s11004-012-9418-1.

Zhabin, A.G., Kremenetskiy, A.A., 1993. The pyrite-pyrrhotite transformation as an ore-concentrating geochemical barrier. Int. Geol. Rev. 35, 359–368. https://doi.org/10.1080/00206819309465534.

Zhang, Y., Zhen, S., Wang, D., Liu, J., Wang, J., Zha, Z., Bai, H., 2022. In situ trace elements and sulfur isotopes of sulfides in the Dabaiyang Te-Au deposit, Hebei Province, China: implications for Au remobilization from pyrite. Ore Geol. Rev. 140, 104626 https://doi.org/10.1016/j.oregeorev.2021.104626.

Zhao, J., Liang, J., Long, X., Li, J., Xiang, Q., Zhang, J., Hao, J., 2018. Genesis and evolution of framboidal pyrite and its implications for the ore-forming process of Carlin-style gold deposits, southwestern China. Ore Geol. Rev. 102, 426–436. https://doi.org/10.1016/j.oregeorev.2018.09.022.

Zhao, Z., Wei, J., Liang, S., Gao, T., 2021. Sulfide remobilization and trace element redistribution during metamorphism and deformation at the Xitieshan Pb-Zn deposit, NW China. Ore Geol. Rev. 136 https://doi.org/10.1016/j.oregeorev.2021.104170.

Zhong, R., Brugger, J., Tomkins, A.G., Chen, Y., Li, W., 2015. Fate of gold and base metals during metamorphic devolatilization of a pelite. Geochem. Cosmochim. Acta 171, 338–352. https://doi.org/10.1016/j.gca.2015.09.013.

Zhu, Y., An, F., Tan, J., 2011. Geochemistry of hydrothermal gold deposits: a review. Geosci. Front. https://doi.org/10.1016/j.gsf.2011.05.006.